doi:10.1038/nature23667

Superparamagnetic enhancement of thermoelectric performance

Wenyu Zhao[1], Zhiyuan Liu[1], Zhigang Sun[1], Qingjie Zhang[1], Ping Wei[1], Xin Mu[1], Hongyu Zhou[1], Cuncheng Li[1], Shifang Ma[1], Danqi He[1], Pengxia Ji[1], Wanting Zhu[1], Xiaolei Nie[1], Xianli Su[1], Xinfeng Tang[1], Baogen Shen[2], Xiaoli Dong[2], Jihui Yang[3], Yong Liu[4] & Jing Shi[4]

The ability to control chemical and physical structuring at the nanometre scale is important for developing high-performance thermoelectric materials[1]. Progress in this area has been achieved mainly by enhancing phonon scattering and consequently decreasing the thermal conductivity of the lattice through the design of either interface structures at nanometre or mesoscopic length scales[2–6] or multiscale hierarchical architectures[7,8]. A nanostructuring approach that enables electron transport as well as phonon transport to be manipulated could potentially lead to further enhancements in thermoelectric performance. Here we show that by embedding nanoparticles of a soft magnetic material in a thermoelectric matrix we achieve dual control of phonon- and electron-transport properties. The properties of the nanoparticles—in particular, their superparamagnetic behaviour (in which the nanoparticles can be magnetized similarly to a paramagnet under an external magnetic field)—lead to three kinds of thermoelectromagnetic effect: charge transfer from the magnetic inclusions to the matrix; multiple scattering of electrons by superparamagnetic fluctuations; and enhanced phonon scattering as a result of both the magnetic fluctuations and the nanostructures themselves. We show that together these effects can effectively manipulate electron and phonon transport at nanometre and mesoscopic length scales and thereby improve the thermoelectric performance of the resulting nanocomposites.

With about two-thirds of all industrial energy consumption being lost as waste heat, there is a compelling need for high-performance thermoelectric materials that can directly and reversibly convert heat to electrical energy[9]. The conversion efficiency of thermoelectric materials is determined by the dimensionless figure of merit $ZT = \alpha^2\sigma T/(\kappa_E + \kappa_L)$, where T is the absolute temperature, α is the Seebeck coefficient, σ is the electrical conductivity, and κ_E and κ_L are the electronic and lattice components of thermal conductivity (κ), respectively. It is extremely hard to simultaneously increase α and σ while reducing κ because of the conflicting properties of thermoelectric materials. To improve the phonon transport properties, various phonon engineering approaches have been used[10–13] to enhance phonon scattering and decrease κ_L. To optimize the electron transport properties, a series of band structure engineering approaches have been developed[14–18] to increase σ, α and/or $\alpha^2\sigma$. The electron and phonon transport properties of In-filled $CoSb_3$ can be simultaneously optimized through coexisting multi-localization transport behaviour[19]. These approaches at atomic and molecular scales have had important roles in manipulating electron and phonon transport of single-phase thermoelectric materials; however, they are not suitable for nanocomposite thermoelectric materials.

Recently, we prepared a magnetic nanocomposite (MNC) thermoelectric material by embedding permanent-magnet $BaFe_{12}O_{19}$ nanoparticles in a thermoelectric matrix, and discovered that these nanoparticles could suppress the deterioration of thermoelectric performance and maintain high ZT values in the intrinsic excitation region through a magnetic transition from ferromagnetism to paramagnetism[20]. However, it has generally been accepted that for all semiconductor materials, including thermoelectric ones, it is necessary to eliminate magnetic impurities to achieve excellent transport properties. This traditional concept has limited the development of MNC thermoelectric materials. But in fact, the Seebeck effect of thermoelectric materials originates from the directional movement of charged carriers from the high-temperature side of the material to the low-temperature side. According to Maxwell's electromagnetic theory, magnetic impurities may change the velocity direction of the moving charged carriers as a result of the Lorentz force, although the velocity magnitude is not affected[21]. The magnetic nanoparticles embedded in thermoelectric materials may act as scattering centres of the carriers and phonons at nanometre and mesoscopic scales. In particular, when the magnetic nanoparticles are in a superparamagnetic state, they cause extra electron and phonon scattering owing to random turning of the magnetic domain. Therefore, introducing superparamagnetic nanoparticles into thermoelectric materials could challenge the traditional concept and provide a new way of manipulating electron and phonon transport simultaneously at nanometre and mesoscopic scales.

We designed and prepared three types of MNC thermoelectric material, consisting of a Pb-free thermoelectric material ($Ba_{0.3}In_{0.3}Co_4Sb_{12}$) as the matrix and soft-magnet transition-metal (Fe, Co or Ni) nanoparticles as the inclusions. As an example, here we report the results of xCo/$Ba_{0.3}In_{0.3}Co_4Sb_{12}$, with $x = 0$, 0.1%, 0.2% or 0.3%, labelled MNC00R, MNC01R, MNC02R or MNC03R, respectively, where the 'R' indicates a repeated sample; see Methods. As shown in Fig. 1 and Extended Data Figs 1 and 2, the Co nanoparticles do not enter into the lattice of the matrix, instead acting as secondary phase impurities that distribute randomly at the interfaces and boundaries of the matrix; these Co nanoparticles are 5–10 nm in diameter.

The magnetic properties of xCo/$Ba_{0.3}In_{0.3}Co_4Sb_{12}$, including magnetization versus magnetic field (M–H) plots, and zero-field-cooling and field-cooling magnetization versus temperature (M–T) plots, are shown in Fig. 2. Co nanoparticles exhibit strong ferromagnetism at room temperature. The matrix (MNC00R) exhibits paramagnetism, in good agreement with the result[22] in Ba-filled $CoSb_3$. The observed paramagnetism also confirms that our preparation process completely avoids Fe contamination. MNC02R has weak ferromagnetism owing to the presence of Co nanoparticles. There is no magnetic transition from ferromagnetism to paramagnetism in xCo/$Ba_{0.3}In_{0.3}Co_4Sb_{12}$ in the temperature range 300–850 K, because the calculated Curie temperature (T_C) of Co nanoparticles with diameters of 5–10 nm is about 1,062–1,216 K (Extended Data Fig. 3b). However, previous

---

[1]State Key Laboratory of Advanced Technology for Materials Synthesis and Processing, Wuhan University of Technology, Wuhan 430070, China. [2]Beijing National Laboratory for Condensed Matter Physics, Institute of Physics of Chinese Academy of Sciences, Beijing 100190, China. [3]Department of Materials Science and Engineering, University of Washington, Seattle, Washington 98195, USA. [4]School of Physics and Technology, Wuhan University, Wuhan 430072, China.

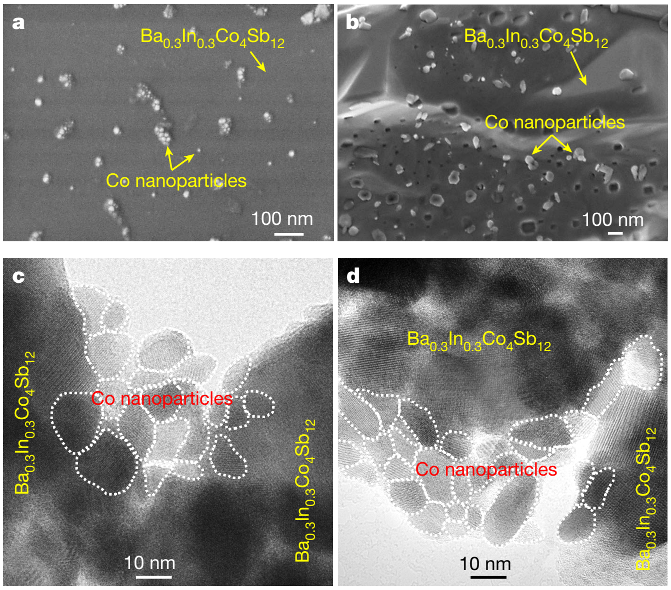

Figure 1 | Microstructures of the as-prepared powders and bulk materials of xCo/$Ba_{0.3}In_{0.3}Co_4Sb_{12}$ with $x = 0.2\%$. **a**, **b**, Field emission scanning electron microscopy images of as-prepared powders and bulk material produced by spark plasma sintering. **c**, **d**, HRTEM images.

results[23] relating to the zero-field-cooling and field-cooling M–T junction of Co nanoparticles indicate that the blocking temperature (T_B) of the magnetic transition from ferromagnetism to superparamagnetism is about 442 K for nanoparticles with the largest diameter of 10 nm (Fig. 2d). The M–H plot for Co nanoparticles at 450 K derived from our experiments, in which both the remnance and coercivity are almost zero, was fitted with the Langevin function, revealing good agreement between the experiment and theory (Fig. 2f). These results indicate that the Co nanoparticles embedded in the $Ba_{0.3}In_{0.3}Co_4Sb_{12}$ matrix are in the ferromagnetic state at temperatures below 442 K and the superparamagnetic state above 442 K.

The electrical transport properties of xCo/$Ba_{0.3}In_{0.3}Co_4Sb_{12}$ at room temperature are summarized in Extended Data Fig. 4 and Extended Data Table 1. MNC01R and MNC02R show a remarkable increase in carrier concentration (n) and substantial decreases in Hall coefficient (R_H) and mobility (μ_H) compared with MNC00R. The increase in σ that we observed originates from the increase in n, according to $\sigma = ne\mu_H$, where e is the elementary charge. In xCo/$Ba_{0.3}In_{0.3}Co_4Sb_{12}$, as secondary phase impurities the Co nanoparticles hardly change the band structure of the matrix; the additional scattering mechanisms induced by Co nanoparticles therefore change only the scattering parameter of xCo/$Ba_{0.3}In_{0.3}Co_4Sb_{12}$ (r_x), but do not affect the effective mass (m^*). Assuming that acoustic phonon scattering is the main carrier scattering mechanism, the scattering parameter of the matrix (r_0) should be $-1/2$ at room temperature. Therefore, r_x can be obtained by calculating $\alpha = [8\pi^2 k_B^2/(3eh^2)]m^*T[\pi/(3n)]^{2/3}(r_x + 1)$ (ref. 24) using the values of α and n measured at room temperature, with k_B the Boltzmann constant and h the Planck constant. The values of r_x follow the same trend as that of α. These results indicate that adding appropriate numbers of Co nanoparticles into the matrix not only provides extra conduction electrons but also enhances the scattering of electrons.

The temperature dependence of all the thermoelectric properties of xCo/$Ba_{0.3}In_{0.3}Co_4Sb_{12}$, including σ, α, κ, κ_L and ZT, are shown in Fig. 3. Having the appropriate number of Co nanoparticles embedded in the matrix simultaneously optimizes three transport parameters σ, α and κ. Compared with the values for MNC00R, the σ and α values for MNC01R and MNC02R are larger, whereas κ and κ_L are much smaller. The ZT values first increase with increasing x and then decrease when $x > 0.2\%$ (Fig. 3d). The maximum ZT value is about 1.8 at 850 K for MNC02, an increase of 32% compared with that of

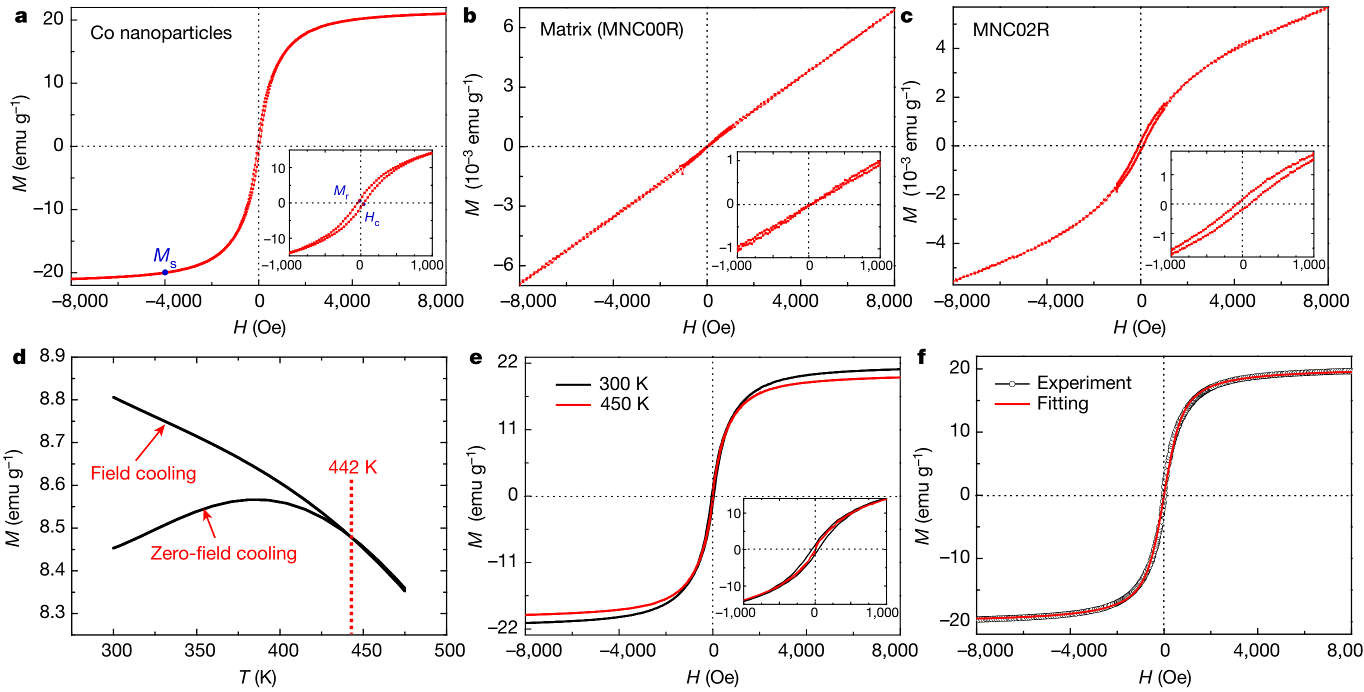

Figure 2 | Measured magnetic properties. **a**–**c**, Magnetization versus magnetic field (M–H) plots for the Co nanoparticles with diameters of 5–10 nm (**a**), the $Ba_{0.3}In_{0.3}Co_4Sb_{12}$ matrix (**b**) and MNC02R (**c**) at room temperature. The points labelled M_s, M_r and H_c represent the saturation magnetization, remnant magnetization and coercive force, respectively. **d**, Zero-field-cooling and field-cooling magnetization versus temperature (M–T) plots for Co nanoparticles with diameters of 5–10 nm. The dashed line at 442 K shows the blocking temperature (T_B) of superparamagnetic transition. **e**, M–H plots for Co nanoparticles with diameters of 5–10 nm at 300 K (black) and 450 K (red). **f**, M–H plot for Co nanoparticles (data points) along with a Langevin fit (red line) at 450 K. The fit yields the saturation magnetic moment of the sample $M_s = 20.31$ emu g^{-1}, the magnetic moment of a particle $\mu = 2.04 \times 10^{-19}$ A m^{-2}, the average volume of the particles $\langle V \rangle = 1.41 \times 10^{-19}$ cm^3 and the average diameter of the particles $D = 6.46$ nm. The insets in **a**–**c** and **e** show the M–H plots near zero field ($H = 0$).

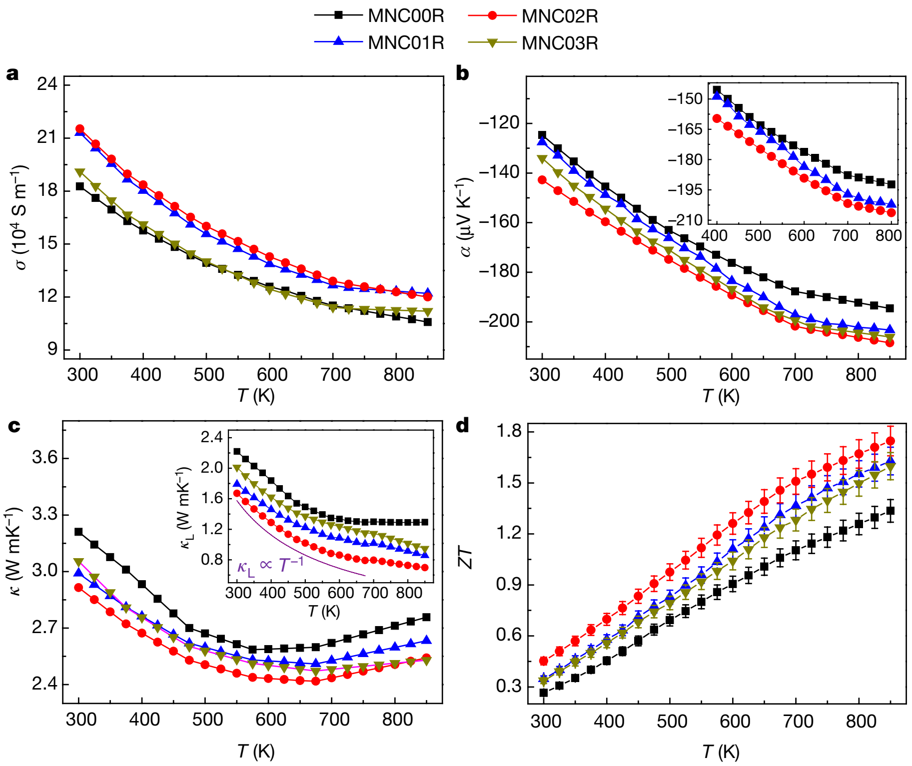

Figure 3 | Electrical and thermal properties in the temperature range 300–850 K. a–d, Temperature dependence of the electric conductivity σ (**a**), Seebeck coefficient α (**b**), thermal conductivity κ (**c**), and figure of merit ZT (**d**) for xCo/$Ba_{0.3}In_{0.3}Co_4Sb_{12}$. The inset in **b** highlights the abnormal temperature dependence of the Seebeck coefficient for MNC01R (blue). The inset in **c** shows the temperature dependence of thermal conductivity of the lattice κ_L; the solid purple curve shows a temperature dependence of T^{-1}, which reveals Umklapp scattering. The error bars in **d** are set to 5%.

the matrix (Extended Data Fig. 5). As shown in the inset in Fig. 3b, the absolute value of α for MNC01R is close to that for the matrix below 450 K, gradually increases above 450 K, and is almost equal to that for MNC02R at 700 K. These features indicate that r_x gradually increases when the temperature is more than 450 K. We calculated the Lorenz number (L) of xCo/$Ba_{0.3}In_{0.3}Co_4Sb_{12}$ in the temperature range 300–850 K using the reduced Fermi energy that we obtained from the measured α in the range 300–850 K and the calculated r_x at room temperature[25]. We used the temperature dependence of L (Extended Data Fig. 4e, f) to calculate κ_E from the Wiedemann–Franz law, $\kappa_E = L\sigma T$; κ_L was obtained using $\kappa_L = \kappa - \kappa_E$. The calculations demonstrate that the additional scattering mechanisms induced by Co nanoparticles are important for determining the x dependences of L, κ_E and κ_L in the temperature range 300–850 K. The low-temperature dependence of κ_L for all of the samples is very close to T^{-1}, indicative of Umklapp scattering. The value of κ_L decreases substantially at high temperature, implying that the phonon scattering that is induced by the Co nanoparticles becomes stronger at high temperature. In addition, the poor thermoelectric properties of MNC03R are due to the presence of p-type $CoSb_2$ impurities.

Our results demonstrate that introducing Co nanoparticles into the thermoelectric matrix leads to new doping and scattering mechanisms that optimize the electron and phonon transport properties simultaneously. To clarify the unusual mechanisms, which also differ from the spin Seebeck contribution to the transverse thermopower in Ni–Pt and MnBi–Au bulk nanocomposites[26], we propose that three thermoelectromagnetic effects are induced by the Co nanoparticles, as shown in Fig. 4.

First, according to the metal–semiconductor contact theory[27], there is a charge transfer of 4s electrons from the Co nanoparticles to the matrix. This charge transfer increases n and then σ for xCo/$Ba_{0.3}In_{0.3}Co_4Sb_{12}$, because the work function of the matrix (φ_s; 's' denotes 'semiconductor') is larger than that of the Co nanoparticles (φ_m; 'm' denotes 'metal'), which have diameters of 5–10 nm (Fig. 4b). The value of φ_s is about 5.26 eV according to ultraviolet photoemission spectroscopy (UPS; Fig. 4a), whereas φ_m is about 5.22–5.11 eV, as calculated using the metal sphere model[28]. The difference between φ_s and φ_m indicates that the interface between the Co nanoparticles and the matrix is an Ohmic contact, and this is confirmed by the current–voltage (I–V) curve that we determined from the experiment (Extended Data Fig. 3g, h). The charge transfer is confirmed by the chemical shift towards lower binding energy in X-ray photoemission spectra (XPS) of Sb 3d core levels (Fig. 4c). The band bending and an interface potential (V_B) that are induced by the charge transfer result in an energy-dependent selective scattering (Fig. 4d). The low-energy conduction electrons are scattered as a result of the interface potential, whereas the high-energy conduction electrons are not affected (Fig. 4e).

Second, an important mechanism for multiple scattering of electrons is induced by superparamagnetic Co nanoparticles. In the ferromagnetic state, the magnetic moment of the Co nanoparticles is rigid and is not affected by the spin of the high-energy conduction electrons; therefore, there is only a single scattering event between the conduction electrons and the Co nanoparticles (Fig. 4f). However, in the superparamagnetic state, the magnetic moment of the Co nanoparticles is no longer rigid and is turned randomly. As a result, in this case the conduction electrons undergo a temperature-dependent multiple scattering (Fig. 4g). The multiple scattering is similar to the Kondo effect[29], in which the conduction electrons undergo multiple scattering owing to the antiferromagnetic coupling. In particular, the multiple scattering due to the superparamagnetism of the Co nanoparticles may explain the abnormal temperature dependences of α for MNC01R in the range 450–700 K. The selective scattering due to the band bending and the multiple scattering from the superparamagnetism of the Co nanoparticles effectively hinders the transport of the electrons. Consequently, the Co nanoparticles (with diameters of 5–10 nm) that are embedded

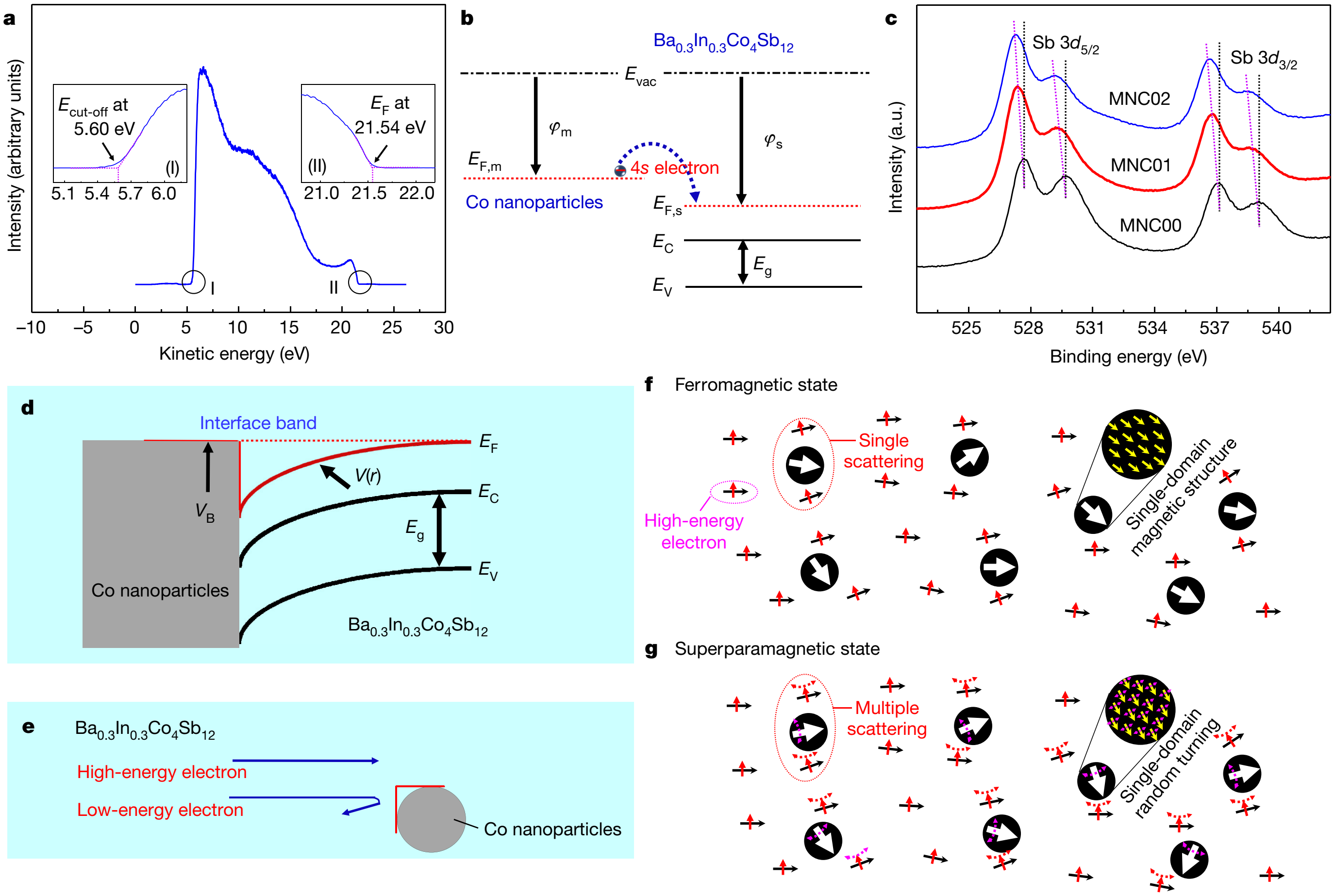

Figure 4 | Thermoelectromagnetic effects induced by Co nanoparticles with diameters of 5–10 nm. a, Ultraviolet photoemission spectroscopy (UPS) spectrum of the $Ba_{0.3}In_{0.3}Co_4Sb_{12}$ matrix; the insets show close-ups of the ringed regions of the spectrum, highlighting the cut-off $E_{\text{cut-off}}$ (I) and Fermi edge E_F (II) of the UPS spectrum. a.u., arbitrary units. **b**, Schematic of the charge transfer of 4*s* electrons from the Co nanoparticles to the matrix; E_{vac} is the vacuum energy, $E_{F,m}$ and $E_{F,s}$ are the Fermi levels of the Co nanoparticles and the matrix, respectively, E_C is the energy of the conduction band minimum, E_V is the energy of the valence band maximum and E_g is the bandgap; φ_m and φ_s are the work functions of the Co nanoparticles and the matrix, respectively. **c**, XPS of Sb $3d_{5/2}$ and $3d_{3/2}$ core levels of xCo/$Ba_{0.3}In_{0.3}Co_4Sb_{12}$ with $x = 0$ (the matrix; MNC00; black), $x = 0.1\%$ (MNC01; red) and $x = 0.2\%$ (MNC02; blue). The black dotted lines show the positions of peaks for the matrix and the purple dotted lines show the positions of peaks for MNC01 and MNC02. **d**, Interface band bending away from the interface induced by the charge transfer of Co 4*s* electrons from the Co nanoparticles (grey) to the matrix (blue). V_B is the interface potential, $V(r)$ is the electrostatic potential and r is the distance between the semiconductor and the interface. **e**, Electron scattering as a result of band bending at the xCo/$Ba_{0.3}In_{0.3}Co_4Sb_{12}$ interfaces. The presence of the interface potential V_B (indicated by the red right angle) causes energy-dependent scatting of electrons. The high-energy electrons are unaffected by V_B, but the low-energy electrons can be strongly scattered. **f**, Single scattering of electrons as a result of the *s*–*d* spin coupling of the ferromagnetic Co nanoparticles, in which the magnetic moment is rigid and not affected by the spin of the high-energy conduction electrons. The small black and red arrows used to illustrate each high-energy electron indicate the direction of travel and spin, respectively. **g**, Multiple scattering of electrons (indicated by the small red dashed arrows) as a result of the random turning of magnetic domains (indicated by the small purple dashed arrows) within the superparamagnetic Co nanoparticles.

in the matrix decrease μ_H and increase r_x, and the increased r_x should therefore be responsible for the increase in α.

Last, the random turning of the magnetic domain for superparamagnetic Co nanoparticles simultaneously enhances the phonon scattering. The large decreases in κ_L for MNC01R and MNC02R are attributed to the extra scattering from the superparamagnetism of the Co nanoparticles and to the enhanced scattering by nanostructures.

We also discovered thermoelectromagnetic effects that led to high thermoelectric performance as a result of superparamagnetism in the MNC thermoelectric materials containing superparamagnetic Fe and Ni nanoparticles (see Extended Data Figs 3, 6–9).

Online Content Methods, along with any additional Extended Data display items and Source Data, are available in the online version of the paper; references unique to these sections appear only in the online paper.

Received 22 November 2016; accepted 20 July 2017.

1. Dresselhaus, M. S. *et al.* New directions for low-dimensional thermoelectric materials. *Adv. Mater.* **19,** 1043–1053 (2007).
2. Zhou, M., Li, J. F. & Kita, T. Nanostructured $AgPb_mSbTe_{m+2}$ system bulk materials with enhanced thermoelectric performance. *J. Am. Chem. Soc.* **130,** 4527–4532 (2008).
3. Hu, Y. J., Zeng, L. P., Minnich, A. J., Dresselhaus, M. S. & Chen, G. Spectral mapping of thermal conductivity through nanoscale ballistic transport. *Nat. Nanotechnol.* **10,** 701–706 (2015).
4. Zhao, W. Y. *et al.* Enhanced thermoelectric performance via randomly arranged nanopores: excellent transport properties of $YbZn_2Sb_2$ nanoporous materials. *Acta Mater.* **60,** 1741–1746 (2012).
5. Fu, C. G. *et al.* Realizing high figure of merit in heavy-band p-type half-Heusler thermoelectric materials. *Nat. Commun.* **6,** 8144 (2015).
6. Luo, Y. B. *et al.* Progressive regulation of electrical and thermal transport properties to high-performance $CuInTe_2$ thermoelectric materials. *Adv. Energy Mater.* **6,** 1600007 (2016).
7. Biswas, K. *et al.* High-performance bulk thermoelectrics with all-scale hierarchical architectures. *Nature* **489,** 414–418 (2012).
8. Wu, H. J. *et al.* Broad temperature plateau for thermoelectric figure of merit $ZT > 2$ in phase-separated $PbTe_{0.7}S_{0.3}$. *Nat. Commun.* **5,** 4515 (2014).
9. Bell, L. E. Cooling, heating, generating power, and recovering waste heat with thermoelectric systems. *Science* **321,** 1457–1461 (2008).
10. Sales, B. C., Mandrus, D. & Williams, R. K. Filled skutterudite antimonides: a new class of thermoelectric materials. *Science* **272,** 1325–1328 (1996).

11. Hsu, K. F. *et al.* Cubic $AgPb_mSbTe_{2+m}$ bulk thermoelectric materials with high figure of merit. *Science* **303,** 818–821 (2004).
12. Poudel, B. *et al.* High-thermoelectric performance of nanostructured bismuth antimony telluride bulk alloys. *Science* **320,** 634–638 (2008).
13. Liu, H. L. *et al.* Copper ion liquid-like thermoelectrics. *Nat. Mater.* **11,** 422–425 (2012).
14. Heremans, J. P. *et al.* Efficiency in PbTe by distortion of the electronic density of states. *Science* **321,** 554–557 (2008).
15. Zhao, L. D. *et al.* Ultrahigh power factor and thermoelectric performance in hole-doped single-crystal SnSe. *Science* **351,** 141–144 (2016).
16. Pei, Y. Z. *et al.* Convergence of electronic bands for high performance bulk thermoelectrics. *Nature* **473,** 66–69 (2011).
17. Liu, W. *et al.* Convergence of conduction bands as a means of enhancing thermoelectric performance of n-type $Mg_2Si_{1-x}Sn_x$ solid. *Phys. Rev. Lett.* **108,** 166601 (2012).
18. Zhao, W. Y. *et al.* Enhanced thermoelectric performance in barium and indium double-filled skutterudite bulk materials via orbital hybridization induced by indium filler. *J. Am. Chem. Soc.* **131,** 3713–3720 (2009).
19. Zhao, W. Y. *et al.* Multi-localization transport behaviour in bulk thermoelectric materials. *Nat. Commun.* **6,** 6197 (2015).
20. Zhao, W. Y. *et al.* Magnetoelectric interaction and transport behaviors in magnetic nanocomposite thermoelectric materials. *Nat. Nanotechnol.* **12,** 55–60 (2016).
21. Pappas, P. T. The original ampere force and Biot–Savart and Lorentz forces. *Il Nuovo Cimento B* **76,** 189–197 (1983).
22. Chen, L. D. *et al.* Anomalous barium filling fraction and *n*-type thermoelectric performance of $Ba_yCo_4Sb_{12}$. *J. Appl. Phys.* **90,** 1864–1868 (2001).
23. Micha, J. S., Dieny, B., Régnard, J. R., Jacquot, J. F. & Sort, J. Estimation of the Co nanoparticles size by magnetic measurements in Co/SiO_2 discontinuous multilayers. *J. Magn. Magn. Mater.* **272–276** (Suppl.), E967–E968 (2004).
24. Cutler, M., Leavy, J. F. & Fitzpatrick, R. L. Electronic transport in semimetallic cerium sulfide. *Phys. Rev.* **133,** A1143–A1152 (1964).
25. Rowe, D. M. & Bhandari, C. M. *Modern Thermoelectric* 26 (Reston Publishing Company, 1983).
26. Boona, S. R., Vandaele, K., Boona, I. N., Mccomb, D. W. & Heremans, J. P. Observation of spin Seebeck contribution to the transverse thermopower in Ni–Pt and MnBi–Au bulk nanocomposites. *Nat. Commun.* **7,** 13714 (2016).
27. Rhoderick, E. H. & Williams, R. H. *Metal–Semiconductor Contacts* 2nd edn, 10–15 (Clarendon Press, 1988).
28. Wood, D. M. Classical size dependence of the work function of small metallic spheres. *Phys. Rev. Lett.* **46,** 749 (1981)
29. Dhara, S., Chowdhury, R. R. & Bandyopadhyay, B. Observation of resistivity minimum at low temperature in Co_xCu_{1-x} ($x \sim 0.17$–0.76) nanostructured granular alloys. *Phys. Rev. B* **93,** 214413 (2016).

Acknowledgements This work was supported by the National Natural Science Foundation of China (numbers 51620105014, 11274248, 51572210 and 51521001) and the National Basic Research Program of China (973-program) (number 2013CB632505). XRD, FESEM, EPMA, HRTEM and Raman-scattering experiments were performed at the Center for Materials Research and Testing at Wuhan University of Technology. Hall measurements were performed at the State Key Laboratory of Advanced Technology for Materials Synthesis and Processing at Wuhan University of Technology. XPS were recorded at the Key Laboratory of Catalysis and Materials Science at the State Ethnic Affair Commission and Ministry of Education of South-Central University for Nationalities. The measurements of static magnetic properties and UPS were performed at the School of Physics and Technology at Wuhan University. We thank S. B. Mu, W. Y. Chen, M. J. Yang, C. H. Shen, X. Q. Liu and Y. Y. Qi for help with structure characterization, J. R. Sun and T. Y. Zhao from the Institute of Physics of CAS for suggestions, and W. Wang from Dongguan University of Technology for preparing magnetic nanoparticles.

Author Contributions W. Zhao and Q.Z. designed a magnetic nanocomposite thermoelectric material for this work. Z.L., C.L., S.M., D.H. and P.J. synthesized the samples. W. Zhao, Z.L., Z.S., X.M., H.Z., X.S., J.S. and X.T. carried out the thermoelectric-property and Hall measurements. W. Zhu, X.N., P.W. and Y.L. performed the electron microscopy analysis and XPS experiments. W. Zhao, P.W., Z.S., Y.L., C.L., J.S., B.S. and X.D. performed the magnetic measurements. W. Zhao, Q.Z., Z.L., Z.S., J.Y. and B.S. conceived the experiments, analysed the results and wrote and edited the manuscript. All authors read the paper and commented on the text.

Author Information Reprints and permissions information is available at www.nature.com/reprints. The authors declare no competing financial interests. Readers are welcome to comment on the online version of the paper. Publisher's note: Springer Nature remains neutral with regard to jurisdictional claims in published maps and institutional affiliations. Correspondence and requests for materials should be addressed to Q.Z. (zhangqj@whut.edu.cn) or J.Y. (jihuiy@uw.edu).

Reviewer Information *Nature* thanks B. Sales and the other anonymous reviewer(s) for their contribution to the peer review of this work.

METHODS

Sample synthesis. Three types of MNC thermoelectric material, xTM/$Ba_{0.3}In_{0.3}Co_4Sb_{12}$ (TM = Co, Fe or Ni) with mass percentage $x = 0$, 0.1%, 0.2%, 0.3% or 0.4%, were prepared. The preparation process of the $Ba_{0.3}In_{0.3}Co_4Sb_{12}$ matrix was based on that reported previously[30], but modified to avoid Fe contamination here. Highly pure metals Co (99.9%, powder), Sb (99.999%, powder), Ba (99%, plate) and In (99.99%, powder) were used as the raw materials of the matrix. Co nanoparticles were prepared by reducing $Co(CH_3COO)_2$ at 533 K using 1,2-hexadecanediol as the reducing agent. Ni nanoparticles were prepared by reducing $Ni(CH_3COO)_2$ at 473 K using oleyl amine as the reducing agent. Fe nanoparticles were prepared by decomposing $Fe(CO)_5$ at 563 K. The preparation process of xTM/$Ba_{0.3}In_{0.3}Co_4Sb_{12}$ MNC thermoelectric materials was as follows. First, the mixtures of raw materials of Co, Fe, Ni and $Ba_{0.3}In_{0.3}Co_4Sb_{12}$ powders were loaded into an enclosed reactor, and thermally reacted to form xTM/$Ba_{0.3}In_{0.3}Co_4Sb_{12}$ MNC particles. To decrease agglomeration of Co, Fe and Ni nanoparticles, all of the MNC particles were thermally treated for 24 h at 473 K by using hexane and ethanol as solvents. Second, the as-prepared MNC powders were sintered into xTM/$Ba_{0.3}In_{0.3}Co_4Sb_{12}$ MNC thermoelectric materials by spark plasma sintering (SPS) (SPS-1050; Dr Sinter) at 923 K under a pressure of 50 MPa in a graphite die. To investigate the reproducibility of the structures and of the measured transport properties of the MNC thermoelectric materials, we prepared two batches of xCo/$Ba_{0.3}In_{0.3}Co_4Sb_{12}$ samples.

Structural characterization. The constituent phases of all of the MNC thermoelectric materials were determined from X-ray diffraction (XRD; PANalytical X'Pert PRO) using Cu Kα radiation ($\lambda = 0.15418$ nm), whereas those of as-prepared Co nanoparticles were determined using Co Kα radiation ($\lambda = 0.17902$ nm). Chemical compositions were quantitatively analysed using electron probe microanalysis (EPMA; JEOL, JXA-8230). The microstructures were examined using a backscattered electron image (BEI) obtained from the EPMA and a secondary electron image (SEI) obtained using field emission scanning electron microscopy (FESEM; Zeiss Ultra-Plus-43-13). High-resolution transmission electron microscopy (HRTEM) images were obtained using a JEM-2100F TEM. X-ray photoemission spectroscopy (XPS) spectra of Sb $3d_{5/2}$ and $3d_{3/2}$ core levels were recorded at a pass energy of 25 eV, step size of 0.05 eV and using 128 scans with a Thermo VG Multilab 2000 spectrometer. Raman spectra were collected using a microscopic confocal-laser Raman spectrometer (Renishaw-Invia), which was excited by a He–Ne laser ($\lambda = 632.8$ nm). The spectral resolution was about 1.5 cm^{-1}. The ultraviolet photoemission spectroscopy (UPS) measurements were performed on a Thermo Fisher ESCALAB 250Xi instrument with an He I radiation source ($h\nu = 21.2$ eV).

Measuring the thermoelectric properties. The σ and α values in the range 300–850 K were measured using the standard four-probe method (Sinkuriko, ZEM-3) in Ar atmosphere; κ was calculated by using the equation $\kappa = \lambda\rho C_p$ (where ρ is the bulk density, C_p is the specific heat capacity and λ is the thermal diffusivity coefficient); λ was measured in the range 300–850 K with a laser flash technique (Netzsch, LFA-427) in a flowing Ar atmosphere; ρ was obtained using an Archimedes method (Sartorius, YDK01); C_p was measured using a TA Q20 differential scanning calorimeter; κ_L was obtained by subtracting the electrical contribution from κ ($\kappa_L = \kappa - \kappa_E$); κ_E is expressed using the Wiedemann–Franz law, $\kappa_E = L\sigma T$. The analysis method for κ_E and κ_L has been used in most heavily doped semiconductor thermoelectric materials with narrow bandgaps, such as[7,10,16,31–33] $LaFe_3CoSb_{12}$, $CeFe_3CoSb_{12}$, $CoSb_3$, $Bi_{0.5}Sb_{1.5}Te_3$, Zn_4Sb_3, $PbTe_{1-x}Se_x$ and SrTe/PbTe. Here, the Lorenz number (L) of xCo/$Ba_{0.3}In_{0.3}Co_4Sb_{12}$ in the range 300–850 K was calculated using the reduced Fermi energy (η) that we obtained from the measured α and the calculated[25] r_x. Uncertainties in σ and κ are ±(5%–7%); uncertainties in α and ZT are ±5%.

Measure the Hall coefficient. The traditional van der Pauw Hall measurement method enables accurate measurement of the Hall effect in semiconductor thermoelectric materials without any magnetic impurity. To avoid impact of the anomalous Hall effect that is induced by the magnetic nanoparticles on the Hall coefficient (R_H) for the MNC thermoelectric materials, we first measured a series of $V_H + V_{aH}$ (where V_H is the Hall voltage and $V_{aH} = i\mu_0 M(H) R_{aH}/d$ is the anomalous Hall voltage) under a fixed current (i) by varying the magnetic fields (H) above the saturation magnetic field (H_s), then linearly fitted the $V_H(H) + V_{aH}(H)$ function to get the slope (k), and finally calculated R_H using $R_H = kd/(i\mu_0)$ (where μ_0 is the vacuum permeability and d is the sample thickness). After getting R_H, the carrier concentration (n) and Hall mobility (μ_H) are calculated using $n = 1/(eR_H)$ and $\mu_H = ne\sigma$, respectively (where e is electron charge). The Hall conductivity (σ_{xy}) is calculated using $\sigma_{xy} = \rho_{xy}/\rho_{xx}^2$, with Hall resistivity $\rho_{xy} = (V_H + V_{aH})\pi d/[i\ln(2)]$ and sample resistivity $\rho_{xx} = 1/\sigma$.

Magnetic properties measurement. The M–H curves at different temperatures and the zero-field-cooling (ZFC) and field-cooling (FC) M–T plots at different magnetic fields were measured using a physical property measurement system (PPMS-9) (Quantum Design). For Co nanoparticles with diameters of 5–10 nm, the measurements of ZFC and FC M–T curves were carried out in the range 300–475 K. The samples were first heated from room temperature to 475 K and subsequently cooled to 300 K without a magnetic field. After the demagnetization process, the samples were heated again from 300 K to 475 K to measure the ZFC M–T curve and cooled from 475 K to 300 K to measure the FC M–T curve under a magnetic field of 400 Oe. For Fe nanoparticles with diameters of 2–5 nm and Ni nanoparticles with diameters of 5–10 nm, the measurements of ZFC and FC M–T curves were carried out in the range 50–350 K. The samples were first heated from room temperature to 350 K and subsequently cooled to 50 K without a magnetic field. After the demagnetization, a magnetic field of 40 Oe for Fe nanoparticles and 20 Oe for Ni nanoparticles was applied during the subsequent heating and cooling processes. The samples were heated again from 50 K to 350 K to measure the ZFC M–T curve, and then cooled from 350 K to 50 K and finally heated from 50 K to 350 K to measure the FC M–T curve.

Effects of Co nanoparticles on structure. XRD patterns of Co nanoparticles and the first batch of xCo/$Ba_{0.3}In_{0.3}Co_4Sb_{12}$ samples ($x = 0$, 0.1%, 0.2% and 0.3%; labelled MNC00, MNC01, MNC02 and MNC03) are shown in Extended Data Fig. 1a, b. The XRD peaks of Co nanoparticles are assigned to the (100), (002), (101) and (102) reflections of Co with hexagonal close-packed structure. All of the recognizable XRD peaks of the xCo/$Ba_{0.3}In_{0.3}Co_4Sb_{12}$ samples can be indexed to those of $CoSb_3$, indicating that the matrix retains good chemical stability in the presence of Co nanoparticles during the SPS process. The close-up XRD patterns in the 2θ range 73°–78° (inset in Extended Data Fig. 1b) indicate that the characteristic diffraction peaks of all the samples that contain Co nanoparticles have no obvious displacement in position compared with those of the matrix. This implies that the Co nanoparticles have no effect on the phase composition of the matrix. No diffraction peaks of Co nanoparticles occur in XRD patterns because the content of the Co nanoparticles is far less than the detection limit of XRD technology (about 1%). Raman spectra of the first batch of xCo/$Ba_{0.3}In_{0.3}Co_4Sb_{12}$ samples are shown in Extended Data Fig. 1c. Four recognizable Raman peaks are almost the same, indicating that Co nanoparticles do not affect the symmetry of the Sb_4 rectangle ring of $CoSb_3$ in the matrix[34]. These results from XRD and Raman spectra clearly show that the Co nanoparticles have not entered into the lattice of the matrix and act only as secondary phase impurities in the MNC thermoelectric materials.

From BEIs (Extended Data Fig. 1d–g), only pores on micrometre scale are observed in MNC00, MNC01 and MNC02, whereas trace impurities of $CoSb_2$ occur in MNC03. The presence of $CoSb_2$ may explain the poor thermoelectric properties of MNC03. FESEM images indicate that the grain boundaries and interfaces are straight and very clean in MNC00 whereas Co nanoparticles with diameters of 5–150 nm are randomly distributed at the interfaces and boundaries of the matrix in xCo/$Ba_{0.3}In_{0.3}Co_4Sb_{12}$, as exemplified by MNC02 in Extended Data Fig. 2a, b. Partial Co nanoparticles are pulled out and form cavities. FESEM images of the second batch of xCo/$Ba_{0.3}In_{0.3}Co_4Sb_{12}$ samples ($x = 0$, 0.1%, 0.2%, 0.3% and 0.4%; label MNC00R, MNC01R, MNC02R, MNC03R and MNC04R; see Extended Data Fig. 2d–g) are very similar to those of the first batch. These results indicate that the microstructures induced by Co nanoparticles in xCo/$Ba_{0.3}In_{0.3}Co_4Sb_{12}$ samples can be reproduced.

HRTEM images show that coarse Co nanoparticles observed in FESEM images are actually composed of fine Co nanoparticles with diameters of 5–10 nm (Fig. 1c, d and Extended Data Fig. 2c). These results demonstrate that the vast majority of Co nanoparticles embedded in the matrix are about 5–10 nm in diameter. To determine the formation mechanism of the coarse Co nanoparticles, we studied the microstructures of as-prepared MNC powders and the sintered samples, as exemplified by MNC02R in Fig. 1. We discover that Co nanoparticles gather into aggregates tens or hundreds of nanometres in size composed of fine Co nanoparticles with diameters of 5–10 nm before the SPS process (see Fig. 1a).

Effects of Co nanoparticles on transport properties. The ΔV_{xy} and Hall conductivity of the two batches of xCo/$Ba_{0.3}In_{0.3}Co_4Sb_{12}$ samples were measured in the range 0.1–1.2 T under a fixed current of 100 mA using the van der Pauw method. As shown in Extended Data Fig. 4, the ΔV_{xy}–H curves for MNC00 and MNC00R (which do not contain Co nanoparticles) just pass through the origin (0, 0), and their fitting lines under H^+ and H^- are almost coincident. However, the ΔV_{xy}–H curves of all the samples that contain Co nanoparticles exhibit linear functional relationships only under high applied magnetic fields. The fitting lines of these plots under high H^+ and H^- are parallel but do not pass through the origin (0, 0), owing to the anomalous Hall effect. Under low magnetic fields, the deviation of ΔV_{xy} from the fitting lines is also due to the anomalous Hall effect.

The charge transport properties of the two batches of xCo/$Ba_{0.3}In_{0.3}Co_4Sb_{12}$ samples at room temperature are listed in Extended Data Table 1. Negative R_H indicates that the majority of carriers in all the samples are electrons exhibiting n-type conduction behaviour. MNC01 and MNC02 exhibit a remarkable increase in n and substantial decreases in R_H and μ_H compared with those of MNC00. According to $\sigma = ne\mu_H$, the increase in σ for MNC01 and MNC02 originates from the remarkable increase in n. MNC03 exhibits a remarkable decrease in n and substantial increases in R_H and μ_H owing to the presence of $CoSb_2$. In the MNC thermoelectric materials, there are two kinds of selective scattering mechanism that are induced by the Co nanoparticles: the energy-dependent scattering of electrons induced by the charge transfer from the Co nanoparticles to the matrix; and the temperature-dependent multiple scattering of high-energy electrons induced by the superparamagnetism of the Co nanoparticles. These selective scattering effects are in fact interface scattering effects between the matrix and the magnetic nanoparticles at nanometre and mesoscopic length scales. Because as secondary phase impurities the Co nanoparticles hardly change the band structure of the matrix, these selective scattering mechanisms change only r_x, and do not affect m^*. The ratio of the scattering parameter $r_x + 1$ for xCo/$Ba_{0.3}In_{0.3}Co_4Sb_{12}$ to $r_0 + 1$ for $Ba_{0.3}In_{0.3}Co_4Sb_{12}$ can be calculated using the α and n values measured at room temperature according to the equation[24] $\alpha = [8\pi^2 k_B^2/(3eh^2)]m^* T[\pi/(3n)]^{2/3}(r_x + 1)$. Therefore, the ratio $(r_x + 1)/(r_0 + 1)$ can be expressed as:

$$\frac{r_x + 1}{r_0 + 1} = \frac{\alpha_x}{\alpha_0}\left(\frac{n_x}{n_0}\right)^{2/3}$$

where α_0 (α_x) and n_0 (n_x) are the α and n values, respectively, of the matrix (of xCo/$Ba_{0.3}In_{0.3}Co_4Sb_{12}$) measured at room temperature. The calculated results are listed in Extended Data Table 1. Assuming acoustic phonon scattering as the main carrier-scattering mechanism, the scattering parameter of the matrix (r_0) should be $-1/2$ at room temperature. Therefore, the scattering parameter r_x at room temperature can be calculated from the $(r_x + 1)/(r_0 + 1)$ ratio and r_0 value. The results are listed in Extended Data Table 1. r_x first increases with increasing x and then greatly decreases when x is more than 0.2%. Therefore, the variation in α induced by the Co nanoparticles is attributed to the change in r_x. Assuming acoustic phonon scattering as the main carrier-scattering mechanism, we calculate the Lorenz number of the matrix and MNC thermoelectric materials in the temperature range 300–850 K using the calculated η and r_x values and

$$L = \left(\frac{k_B}{e}\right)^2 \left\{ \frac{(r + 7/2)F_{r+5/2}(\eta)}{(r + 3/2)F_{r+1/2}(\eta)} - \left[\frac{(r + 5/2)F_{r+3/2}(\eta)}{(r + 3/2)F_{r+1/2}(\eta)}\right]^2 \right\}$$

where $F_n(\eta)$ is the nth-order Fermi integral:

$$F_n(\eta) = \int_0^\infty \frac{\chi^n}{1 + e^{\chi - \eta}} d\chi, \ \eta = \frac{E_F}{k_B T}$$

For most heavily doped semiconductor thermoelectric materials with narrow bandgaps, η can be derived from the measured Seebeck coefficient (α) and r_x on the basis of a single-band approximation:

$$\alpha = \pm \frac{k_B}{e}\left[\frac{(r + 5/2)F_{r+3/2}(\eta)}{(r + 3/2)F_{r+1/2}(\eta)} - \eta\right]$$

Extended Data Fig. 4e, f shows the temperature dependence of L for the first (MNC00, MNC01, MNC02 and MNC03) and second (MNC00R, MNC01R, MNC02R, MNC03R, MNC04R) batches of MNC thermoelectric materials in the range 300–850 K. The L values for all of the samples decrease with increasing temperature; however, the degree of decrease is less than 10%. L first increases with increasing x and then decreases substantially when x is more than 0.2%.

As shown in Extended Data Fig. 5, the similar temperature dependences of σ imply that the n values for MNC01 and MNC02 do not differ much in the entire range 300–850 K, indicating that soft-magnet Co nanoparticles have no 'electron repository' role, as do the permanent-magnet $BaFe_{12}O_{19}$ nanoparticles in $x$$BaFe_{12}O_{19}$/$Ba_{0.3}In_{0.3}Co_4Sb_{12}$ (ref. 20). The absolute value of α for MNC01 is close to that for the matrix below 450 K, gradually increases above 450 K, and is almost equal to that of MNC02 at 700 K (inset in Extended Data Fig. 5b). This implies that r_x gradually increases when the temperature is more than 450 K. Unlike the majority of thermoelectric materials, for which the relationship between σ and α is usually reciprocal, the values of σ and α for MNC01 and MNC02 simultaneously increase in the entire range 300–850 K compared with those for the matrix. In addition, the values of σ and α for MNC03 are much less than those for MNC02 owing to the large decrease in n and r_x and the remarkable increase in μ_H, which can be explained by the presence of $CoSb_2$ (see Extended Data Fig. 1g).

The $\alpha^2\sigma$ values for MNC01 and MNC02 are much higher than those for the matrix in the entire range 300–850 K (see Extended Data Fig. 5c), demonstrating that optimizing the number of Co nanoparticles can greatly increase $\alpha^2\sigma$. The largest value of $\alpha^2\sigma$ is 5.5 mW m^{-1} K^{-2} at 575 K for MNC02. As shown in Extended Data Fig. 5d, the κ values for all the samples that contain Co nanoparticles are very similar, but are much less than those for the matrix in the range 300–850 K. The κ_E values first increase and then decrease substantially when $x > 0.2\%$ (inset in Extended Data Fig. 5d). The κ_E values for MNC01 and MNC02 are larger than that for the matrix, which is attributed to the contribution of the larger σ. The κ_L values for all the samples that contain Co nanoparticles (Extended Data Fig. 5e) rapidly decrease in the range 300–675 K owing to the enhanced lattice vibration and slowly increase above 675 K owing to the compromise between the bipolar thermal diffusion and the enhanced phonon scattering that is induced by the lattice vibration. The κ_L values for all the samples that contain Co nanoparticles are much lower than that for the matrix in the range 300–850 K, indicating that Co nanoparticles embedded in the $Ba_{0.3}In_{0.3}Co_4Sb_{12}$ matrix behave as strong phonon-scattering centres. The temperature dependence of κ_L is very close to T^{-1} for all the samples in the range 300–675 K, indicating that the phonon–phonon Umklapp scattering is dominant. Compared with the matrix, the κ_L values for all the samples that contain Co nanoparticles decrease substantially at high temperature, implying that the phonon scattering induced by the Co nanoparticles becomes stronger at high temperature. However, both the κ and κ_L values for MNC03 are higher than those for MNC01 and MNC02 in the range 300–850 K, owing to the presence of $CoSb_2$, which has high thermal conductivity.

The ZT values of xCo/$Ba_{0.3}In_{0.3}Co_4Sb_{12}$ (Extended Data Fig. 5f) first increase with increasing x and then decrease when $x > 0.2\%$. The maximum ZT value is about 1.8 at 850 K for MNC02, an increase of 32% compared with that of the matrix. The Co nanoparticles simultaneously optimize the three transport parameters σ, α and κ in xCo/$Ba_{0.3}In_{0.3}Co_4Sb_{12}$.

The R_H, μ_H, n, σ and r_x values of the second batch of samples (MNC00R–MNC04R) at room temperature are listed in Extended Data Table 1. The temperature dependence of σ, α, $\sigma\alpha^2$, κ, κ_L, κ_E and ZT for these samples is shown in Extended Data Fig. 5g–l. All the transport properties of these samples exhibit the same evolution laws with the x as those of the first batch of samples (shown in Extended Data Fig. 5a–f and Extended Data Table 1), indicating that all of the thermoelectric properties that we have reported are reproducible.

We also investigated the thermoelectric properties of MNC00R and xTM/$Ba_{0.3}In_{0.3}Co_4Sb_{12}$ with $x = 0.2\%$ and TM = Fe, Co and Ni (labelled MNC02R_Fe, MNC02R_Co and MNC02R_Ni, respectively) in the range 300–850 K. As shown in Extended Data Fig. 6a–d, the introduction of Fe, Co and Ni nanoparticles into the $Ba_{0.3}In_{0.3}Co_4Sb_{12}$ matrix produces the same favourable combination of simultaneously enhancing α, increasing σ and reducing κ_L.

Magnetic transition and superparamagnetism of Fe, Co and Ni nanoparticles. Theoretically, soft-magnet transition-metal Fe, Co and Ni nanoparticles can undergo a magnetic transition from ferromagnetism to superparamagnetism when the magnetocrystalline anisotropy energy ($K_1 V$) is comparable to or smaller than the thermal energy ($k_B T$). The volume of spherical nanoparticles with diameter D is $V = \pi D^3/6$. The critical diameter (D_C) of these nanoparticles for undergoing the superparamagnetic transition under different temperatures is

$$D_C = \left(\frac{6k_B T}{\pi K_1}\right)^{1/3}$$

where $K_1 = K_1 \sin\theta^2 + K_2 \sin\theta^4$ and $k_B = 1.38 \times 10^{-23}$ J K^{-1}. Using values of K_1 and K_2 for Co from ref. 35, we can calculate K_1 for Co in the range 298–673 K when $\theta = \pi/2$. Therefore, we can use the above equation to calculate D_C for soft-magnet Co nanoparticles, which can produce the superparamagnetism transition in the range 298–673 K. The temperature dependence of D_C for Co nanoparticles is shown in Extended Data Fig. 3a. Using values of K_1 and K_2 for Fe from ref. 36 and for Ni from ref. 37, we can calculate D_C for Fe and Ni nanoparticles; the results are shown in Extended Data Fig. 3c, e.

A ferromagnetic nanoparticle must have another magnetic transition (besides the superparamagnetic transition) from ferromagnetism to paramagnetism. On the basis of a size-dependent cohesive-energy model[38], T_C can be expressed in the form

$$\frac{T_C(D)}{T_C(\infty)} = \left[1 - \frac{1}{2D/(ch) - 1}\right] \exp\left[-\frac{2S_b}{3R}\frac{1}{2D/(ch) - 1}\right]$$

where '∞' denotes the bulk value ($T_C(\infty) \approx 1{,}388$ K for Co, 1,043 K for Fe and 631 K for Ni; ref. 39), $S_b \approx 117.62$ J mol^{-1} K^{-1} for Co, 111.52 J mol^{-1} K^{-1} for Fe and 116.22 J mol^{-1} K^{-1} for Ni (ref. 40), $R = 8.314$ J mol^{-1} K^{-1}, $h = 0.2497$ nm for Co, 0.2483 nm for Fe and 0.2492 nm for Ni (refs 41, 42) and c is a constant that reflects the normalized surface area (for nanoparticles, $c = 1$). Using these parameters, we calculate T_C for Co, Fe and Ni nanoparticles with diameters of 1–150 nm using the above equation; the results are shown in Extended Data Fig. 3b, d, f.

Using Extended Data Fig. 3, we can predict the blocking temperature (T_B) of the superparamagnetic transition and T_C for the paramagnetic transition of Co, Fe and Ni nanoparticles, if their diameters have been determined. TEM images (see Extended Data Figs 7d, 8d and 9d) show that the diameters of Co, Fe and Ni nanoparticles are about 5–10 nm, 2–5 nm and 5–10 nm, respectively. For Co nanoparticles with diameters of 5–10 nm, the theoretical T_B for the magnetic transition from ferromagnetism to superparamagnetism is about 450–550 K, whereas the theoretical T_C is more than 1,000 K. Therefore, the superparamagnetic transition can occur in xCo/$Ba_{0.3}In_{0.3}Co_4Sb_{12}$ in the range 300–850 K but the paramagnetic one cannot. For Fe nanoparticles with diameters of 2–5 nm, the theoretical T_B is about 250–350 K and T_C is about 400–800 K. Therefore, in xFe/$Ba_{0.3}In_{0.3}Co_4Sb_{12}$ not only superparamagnetic transition can occur but also the paramagnetic one in the range 300–850 K. For Ni nanoparticles with diameters of 5–10 nm, the theoretical T_B is about 150–300 K and T_C is about 400–800 K. Therefore, in xNi/$Ba_{0.3}In_{0.3}Co_4Sb_{12}$ the paramagnetic transition can occur in the range 300–850 K, but the superparamagnetic one cannot because the material is already in the superparamagnetic state before the paramagnetic transition. These theoretical results agree well with the experimental evidence of the superparamagnetism of the Co, Fe and Ni nanoparticles (see Extended Data Figs 7–9).

The FC and ZFC M–T curves for the Co nanoparticles with diameters of 5–10 nm (see Extended Data Fig. 7) show that $T_B \approx 442$ K. This result is in good agreement with the results from the experimental M–H curves at 300 K and 450 K and the Langevin fitting at 450 K. The Langevin fitting results show that for Co nanoparticles the saturation magnetic moment of the sample is $M_0 \approx 20.31$ emu g^{-1}, the magnetic moment of a particle is $\mu \approx 2.04 \times 10^{-19}$ A m^{-2}, the average volume of the particles is $\langle V \rangle \approx 1.41 \times 10^{-19}$ cm^3 and the average diameter of the particles is about 6.46 nm. The fitted diameter is well matched by that observed using TEM, as shown in Extended Data Fig. 7d. These results show that Co nanoparticles with diameters of 5–10 nm embedded in the $Ba_{0.3}In_{0.3}Co_4Sb_{12}$ matrix are in the ferromagnetic state below 442 K and the superparamagnetic state above 442 K.

The FC and ZFC M–T curves for Fe nanoparticles with diameters of 2–5 nm (Extended Data Fig. 8) and Ni nanoparticles with diameters of 5–10 nm (Extended Data Fig. 9) show that $T_B \approx 295$ K and 298 K, respectively. These results are in good agreement with those derived from the experimental M–H plots at 50 K and 350 K and the Langevin fitting at 350 K. The fitted diameters are also well matched by those observed using TEM, as shown in Extended Data Figs 8d and 9d. These results show that Fe and Ni nanoparticles embedded in the $Ba_{0.3}In_{0.3}Co_4Sb_{12}$ matrix are in the ferromagnetic state below T_B and the superparamagnetic state above T_B.

As shown in Extended Data Fig. 6e–h, at room temperature, MNC00R exhibits paramagnetism, MNC02R_Fe and MNC02R_Ni exhibit paramagnetism-like behaviour and MNC02R_Co exhibits weak ferromagnetism. The paramagnetism of MNC00R confirms that our modified preparation process completely avoids Fe contamination. At 300 K, the paramagnetism-like behaviour of MNC02R_Fe and MNC02R_Ni is due the Fe and Ni nanoparticles being in the superparamagnetic state; the ferromagnetism of MNC02R_Co originates from the Co nanoparticles being in the ferromagnetic state.

Effects of Co nanoparticles on the interfaces. Figure 4a shows the UPS spectrum of the matrix; the insets show close-ups of the ringed regions of the spectrum, highlighting the cut-off $E_{\text{cut-off}}$ (I) and Fermi edge E_F (II) of the UPS spectrum. The inelastic cut-off position ('I' circle) and the Fermi edge position ('II' circle) of the matrix were determined using a linear extrapolation method[43]. The kinetic energy of the inelastic cut-off ($E_{\text{cut-off}}$) and of the Fermi edge (E_F) are about 5.60 eV and 21.54 eV, respectively. Therefore, the spectrum width (L) of the UPS spectrum for the matrix was obtained by subtracting $E_{\text{cut-off}}$ from E_F ($L = E_F - E_{\text{cut-off}} \approx 15.94$ eV). The work function of the matrix is[44] $\varphi_s = h\nu - L$, where $h\nu$ is the photon energy. Because $h\nu$ is constant, and equal to about 21.2 eV here, $\varphi_s \approx 5.26$ eV.

The work function of Co nanoparticles (in eV) is calculated using the equation for spherical metal particles[28]:

$$\varphi_m(R) = \varphi_\infty + \frac{5.40}{R}$$

where φ_∞ is the work function of the bulk metals and R is the radius of the particles (in Å). φ_∞ for bulk Co is 5.00 eV (ref. 45) and R for Co nanoparticles is about 2.5–5 nm (see Extended Data Fig. 7d). Therefore, $\varphi_m \approx 5.22$–5.11 eV. The difference between φ_m and φ_s indicates that the interfaces between the Co nanoparticles and the matrix are Ohmic contacts, which is helpful in maintaining low interface resistance. According to the contact theory between a metal and a semiconductor[27], there is a charge transfer of 4s electrons from the Co nanoparticles to the matrix because $\varphi_m < \varphi_s$ (Fig. 4b). The charge transfer mechanism not only explains the chemical shift towards lower binding energy in the XPS of Sb 3d core levels (Fig. 4c) and the increases in n and σ, but also the band bending and an interface potential (Fig. 4d).

To demonstrate the Ohmic contact between the Co nanoparticles and the matrix, we performed an additional experiment (Extended Data Fig. 3g, h). Co was first evaporated onto the matrix, and then Cu electrodes were connected with the Co using a tin solder. The I–V curve is a straight line through the origin (0, 0), demonstrating a good and stable Ohmic contact between the Co and the matrix, consistent with the analytical result from the work functions of the Co nanoparticles and the matrix.

Data availability. The data that support the findings of this study are available from corresponding author Q.Z. on reasonable request.

30. Zhao, W. Y. *et al.* Synthesis and high temperature transport properties of barium and indium double-filled skutterudites $Ba_xIn_yCo_4Sb_{12-z}$. *J. Appl. Phys.* **102,** 113708 (2007).
31. Fitsul, V. I. *Heavily Doped Semiconductors* 139–169 (Plenum Press, 1969).
32. Snyder, G. J., Christensen, M., Nishibori, E. J., Caillat, T. & Iversen, B. B. Disordered zinc in Zn_4Sb_3 with phonon glass, electron crystal thermoelectric properties. *Nat. Mater.* **3,** 458–463 (2004).
33. Kim, S. I. *et al.* Dense dislocation arrays embedded in grain boundaries for high-performance bulk thermoelectrics. *Science* **348,** 109–114 (2015).
34. Nolas, G. S., Kendziora, C. A. & Takizawa, H. Polarized Raman-scattering study of Ge and Sn-filled $CoSb_3$. *J. Appl. Phys.* **94,** 7440–7444 (2003).
35. Sucksmith, W. & Thompson, J. E. The magnetic anisotropy of cobalt. *Proc. R. Soc. Lond. A* **225,** 362–375 (1954).
36. Bozorth, R. M. Directional ferromagnetic properties of metals. *J. Appl. Phys.* **8,** 575–588 (1937).
37. Tatsumoto, E., Okamoto, T., Iwata, N. & Kadena, Y. Temperature dependence of the magnetocrystalline anisotropy constants K_1 and K_2 of nickel. *J. Phys. Soc. Jpn.* **20,** 1541–1542 (1965).
38. Yang, C. C. & Jiang, Q. Size and interface effects on critical temperatures of ferromagnetic, ferroelectric and superconductive nanocrystals. *Acta Mater.* **53,** 3305–3311 (2005).
39. Mohn, P. & Wohlfarth, E. P. The Curie temperature of the ferromagnetic transition metals and their compounds. *J. Phys. F* **17,** 2421–2430 (1987).
40. Edgar, E. L. *Periodic Table of the Elements* 1 (Gaston, 1993).
41. King, H. W. in *Physical Metallurgy* 3rd edn (eds Cahn, R. W. & Haasen, P.) 59–63 (Amsterdam, 1983).
42. Jiang, Q. & Lang, X. Y. Glass transition of low-dimensional polystyrene. *Macromol. Rapid Commun.* **25,** 825–828 (2004).
43. Gao, Y. L. Surface analytical studies of interfaces in organic semiconductor devices. *Mater. Sci. Eng. Rep.* **68,** 39–87 (2010).
44. Ertl, G. & Küppers, J. *Low Energy Electrons and Surface Chemistry* 87–143 (VCH, 1985).
45. Michaelson, H. B. The work function of the elements and its periodicity. *J. Appl. Phys.* **48,** 4729–4733 (1977).

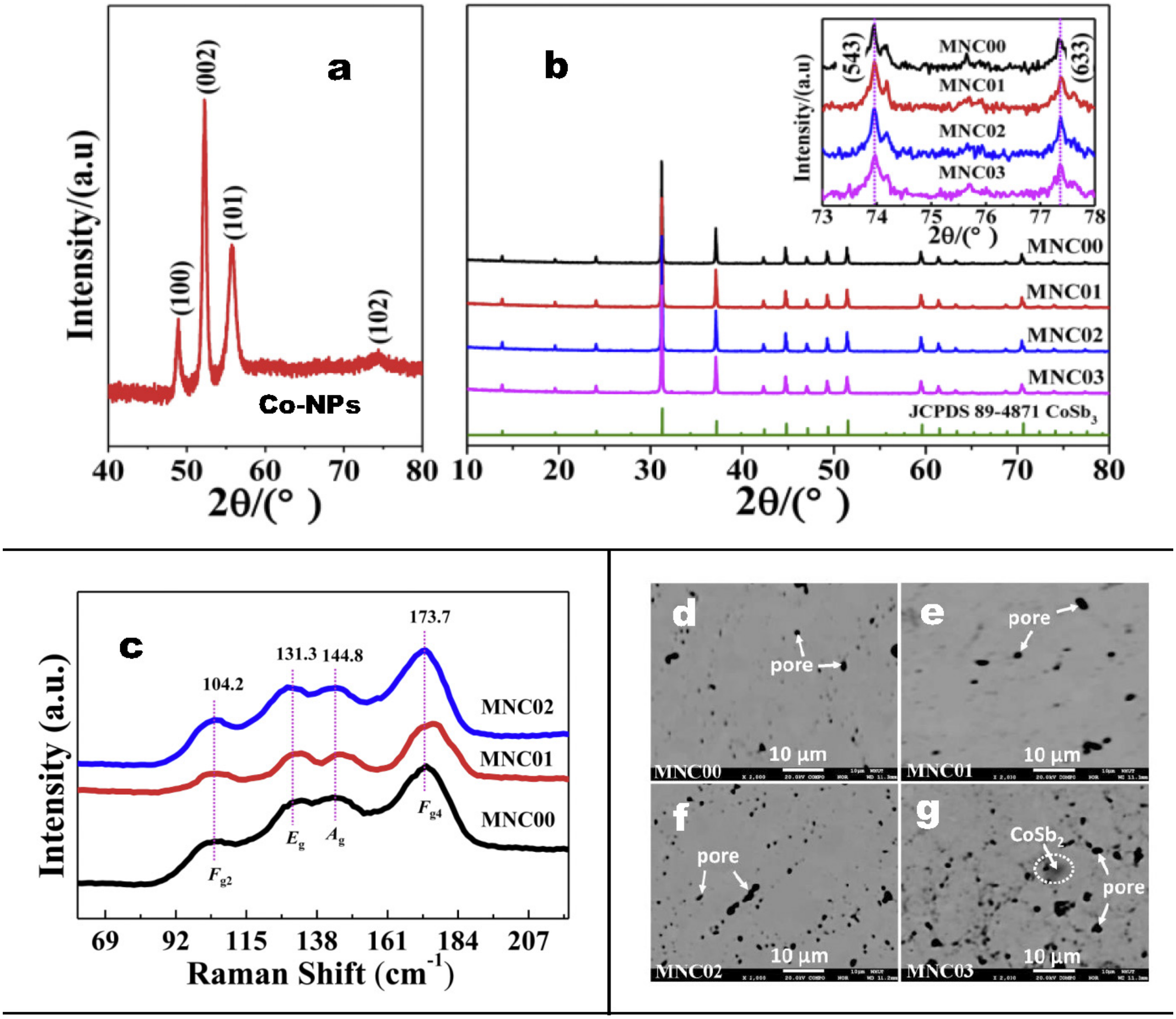

Extended Data Figure 1 | Effect of Co nanoparticles on structure. a, XRD patterns of Co nanoparticles. **b**, XRD patterns of the first batch of xCo/Ba$_{0.3}$In$_{0.3}$Co$_4$Sb$_{12}$ ($x = 0$, 0.1%, 0.2% and 0.3%; labelled MNC00, MNC01, MNC02 and MNC03). **c**, Raman spectra of the first batch of samples. **d**–**g**, BEIs of the first batch of samples.

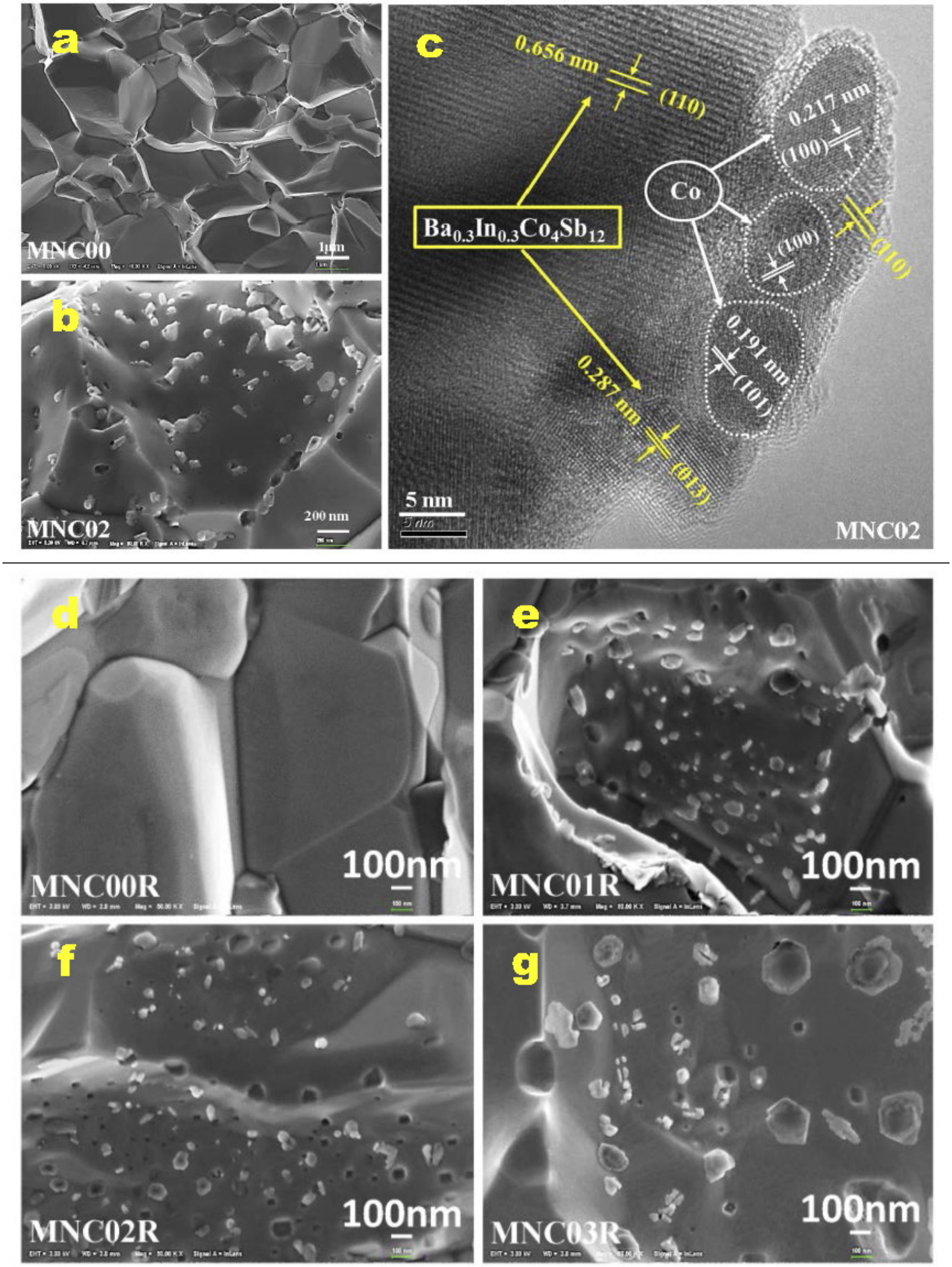

Extended Data Figure 2 | Effect of the Co nanoparticles on microstructure. **a**, **b**, FESEM images of MNC00 (**a**) and MNC02 (**b**). **c**, HRTEM image of MNC02. **d**–**g**, FESEM images of MNC00R, MNC01R, MNC02R and MNC03R, respectively.

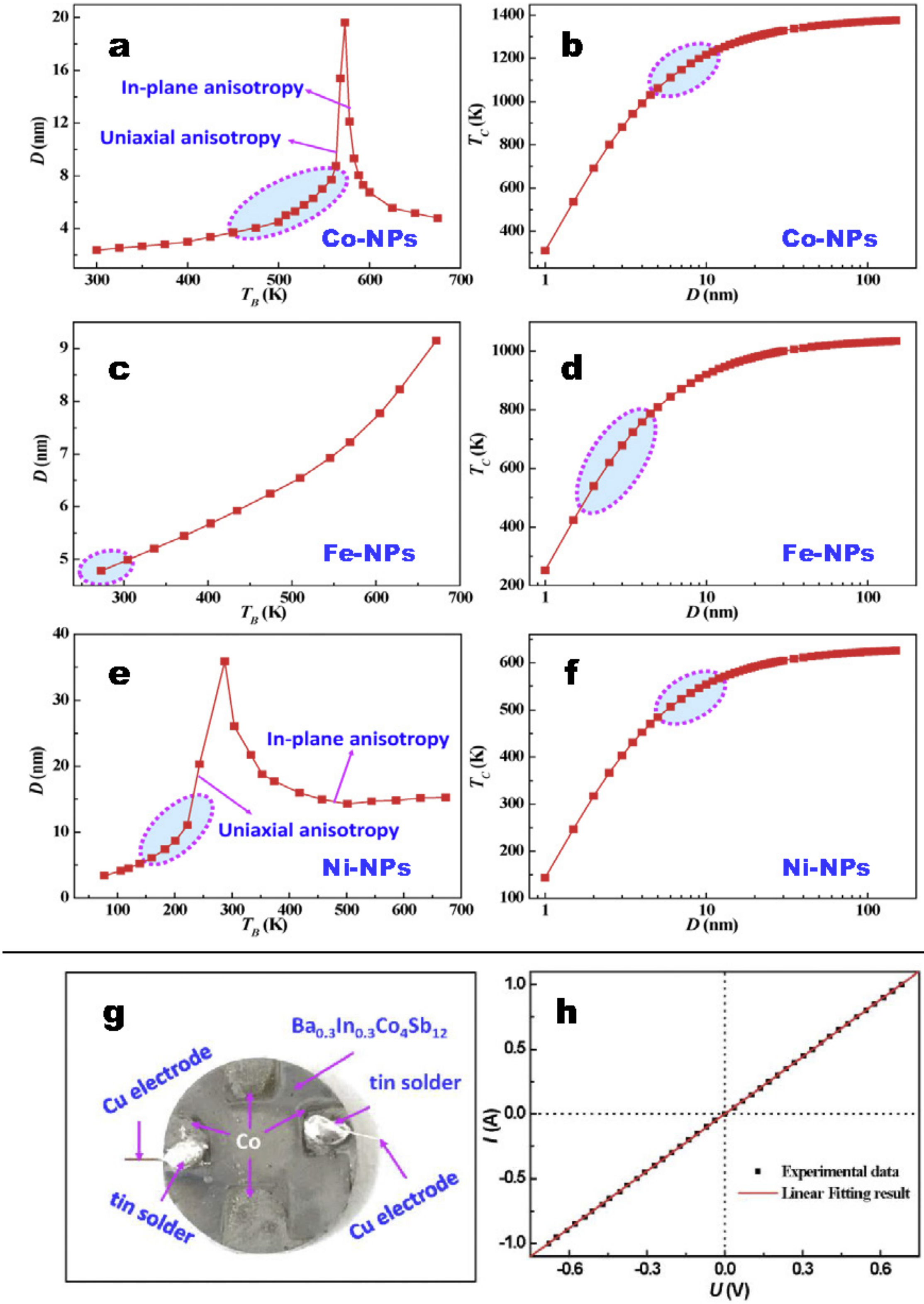

Extended Data Figure 3 | Theoretical blocking temperature (T_B) and Curie temperature (T_C), and the Ohmic contact experiment. **a**, **c**, **e**, Theoretical T_B dependence of the critical diameter D_C. **b**, **d**, **f**, Theoretical T_C dependence of the critical diameter D_C. The oval shaded areas delineated by dotted lines indicate the range of T_B and T_C for the Co and Ni nanoparticles diameters of 5–10 nm and the Fe nanoparticles diameters of 2–5 nm. **g**, Experimental sample for measuring the Ohmic contact between Co and filled skutterudite. Co was first evaporated onto the matrix and then Cu electrodes were connected with the Co using a tin solder. **h**, *I*–*V* plot: a straight line through the origin (0, 0), demonstrating a good and stable Ohmic contact between the Co and the matrix, consistent with the analytical result from the work functions of the Co nanoparticles and the matrix.

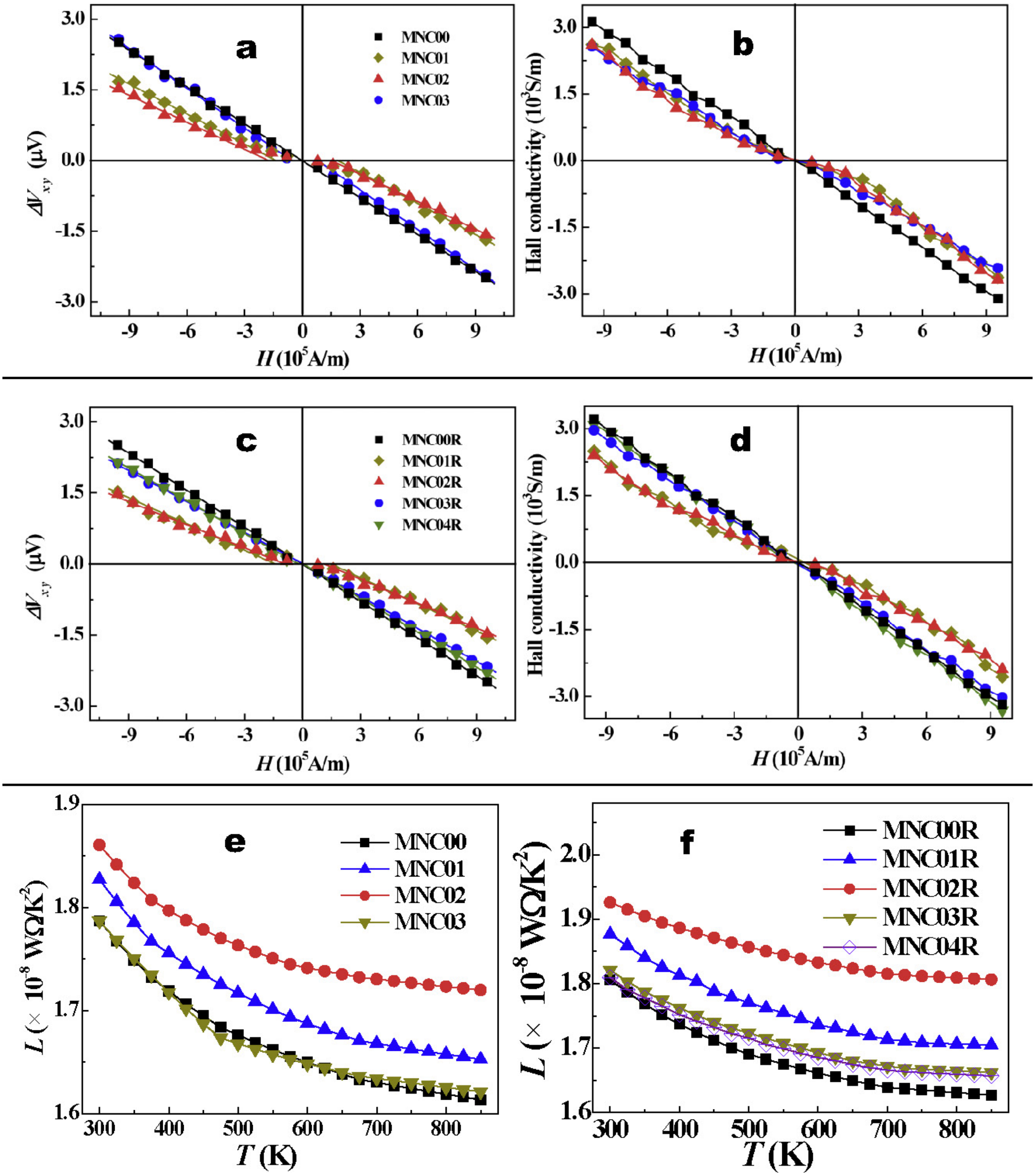

Extended Data Figure 4 | Experimental data from Hall measurements and theoretical Lorenz number (L). **a**, **b**, The first batch of samples. **c**, **d**, The second batch of samples. The measuring current remains unchanged at 100 mA. The magnetic field is varied in the range 0.1–1.2 T. The ΔV_{xy} values measured in the range 0.5–1.2 T are used to linearly fit the Hall coefficient. **e**, **f**, Temperature dependence of L for the first (**e**; MNC00, MNC01, MNC02 and MNC03) and second (**f**; MNC00R, MNC01R, MNC02R, MNC03R and MNC04R) batches of MNC thermoelectric materials batch in the range 300–850 K.

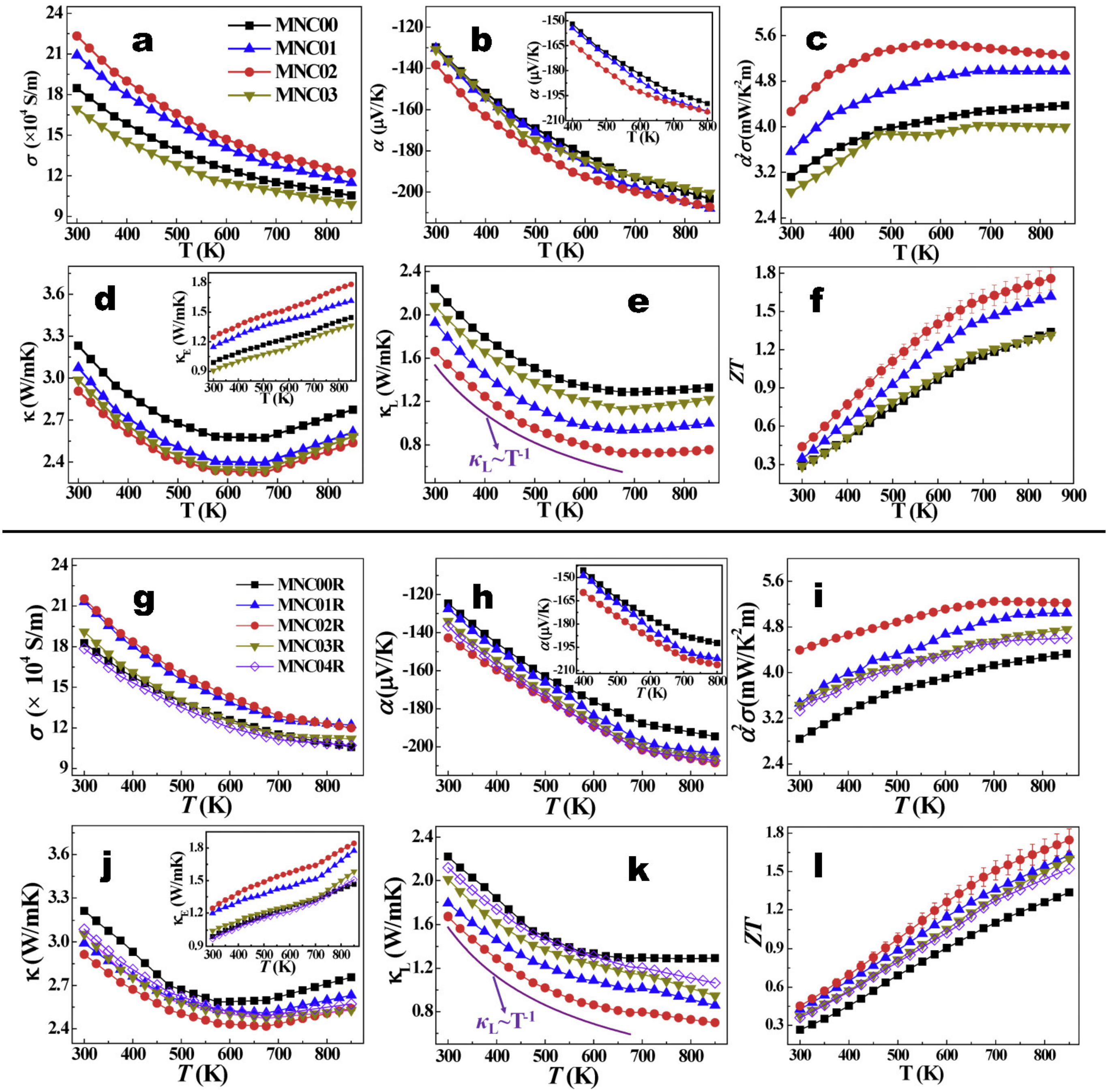

Extended Data Figure 5 | Effect of the Co nanoparticles on the electrical and thermal transport properties in the range 300–850 K. a–f, The first batch of samples. **g–l**, The second batch samples. **a–l**, Temperature dependence of the electric conductivity σ (**a**, **g**), the Seebeck coefficient α (**b**, **h**), the power factor $\alpha^2\sigma$ (**c**, **i**), the thermal conductivity κ (**d**, **j**), lattice thermal conductivity κ_L (**e**, **k**) and ZT (**f**, **l**). The insets in **d** and **j** show the temperature dependence of the carrier thermal conductivity κ_E. The error bars in **f** and **l** are set to 5%.

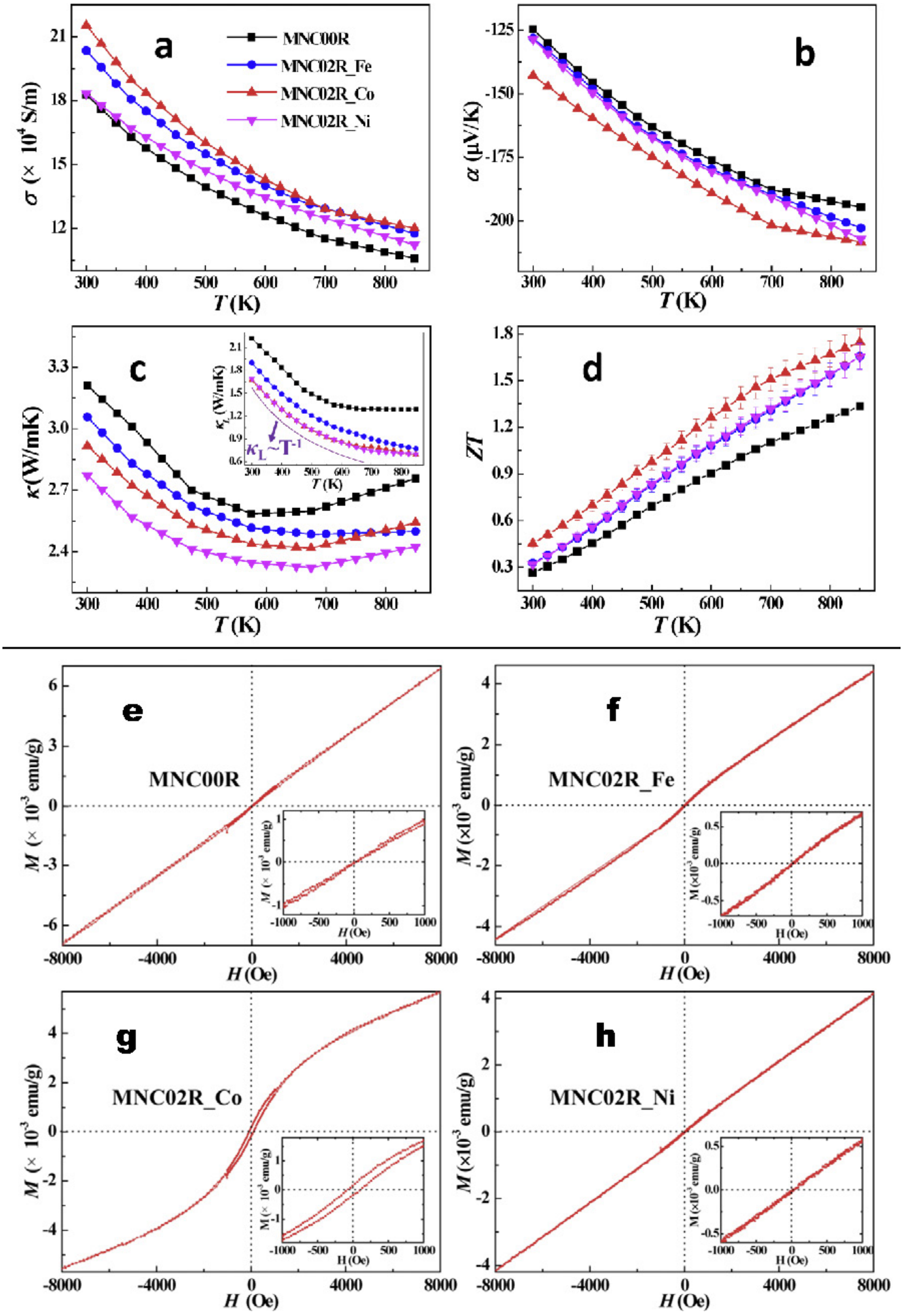

Extended Data Figure 6 | Effect of the Fe, Co and Ni nanoparticles on the thermoelectric and magnetic properties. a–d, Temperature dependence of the electric conductivity σ (**a**) Seebeck coefficient α (**b**), thermal conductivity κ (**d**) and ZT for MNC00R and xTM/$Ba_{0.3}In_{0.3}Co_4Sb_{12}$ (TM = Fe, Co or Ni) with $x = 0.2\%$, labelled MNC02R_Fe, MNC02R_Co and MNC02R_Ni, respectively. The inset in **c** shows the temperature dependence of the lattice thermal conductivity κ_L. **e–h**, M–H curves at room temperature. The insets in **e–h** show close-ups near zero field.

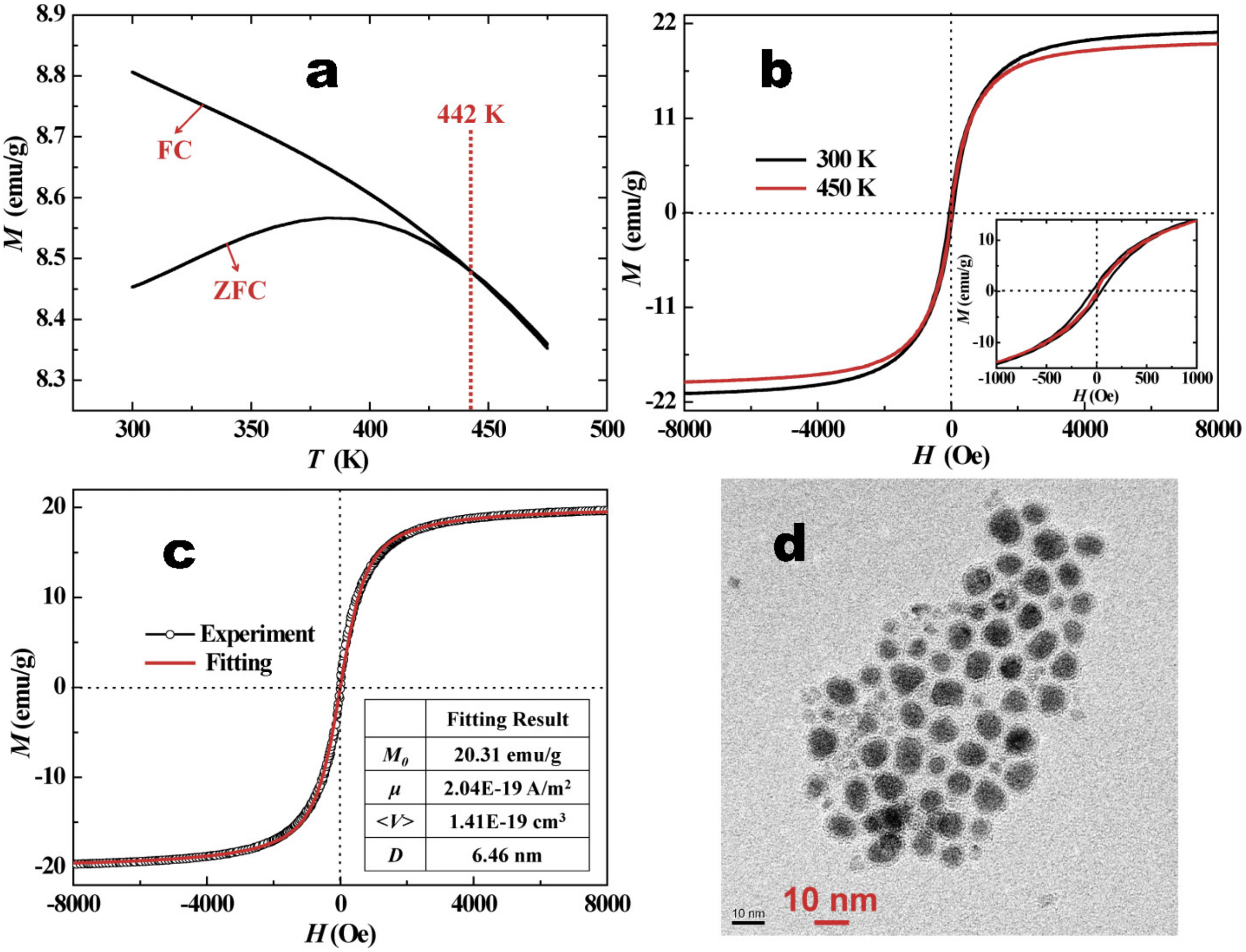

Extended Data Figure 7 | Experimental evidence of the superparamagnetism of the Co nanoparticles with diameters of 5–10 nm. **a**, ZFC and FC *M*–*T* curves. **b**, *M*–*H* curves at 300 K and 450 K. **c**, Langevin fitting of the *M*–*H* curves at 450 K. **d**, TEM image of the Co nanoparticles. The inset in **b** shows the *M*–*H* curves near zero field. The inset in **c** shows the results of the Langevin fitting.

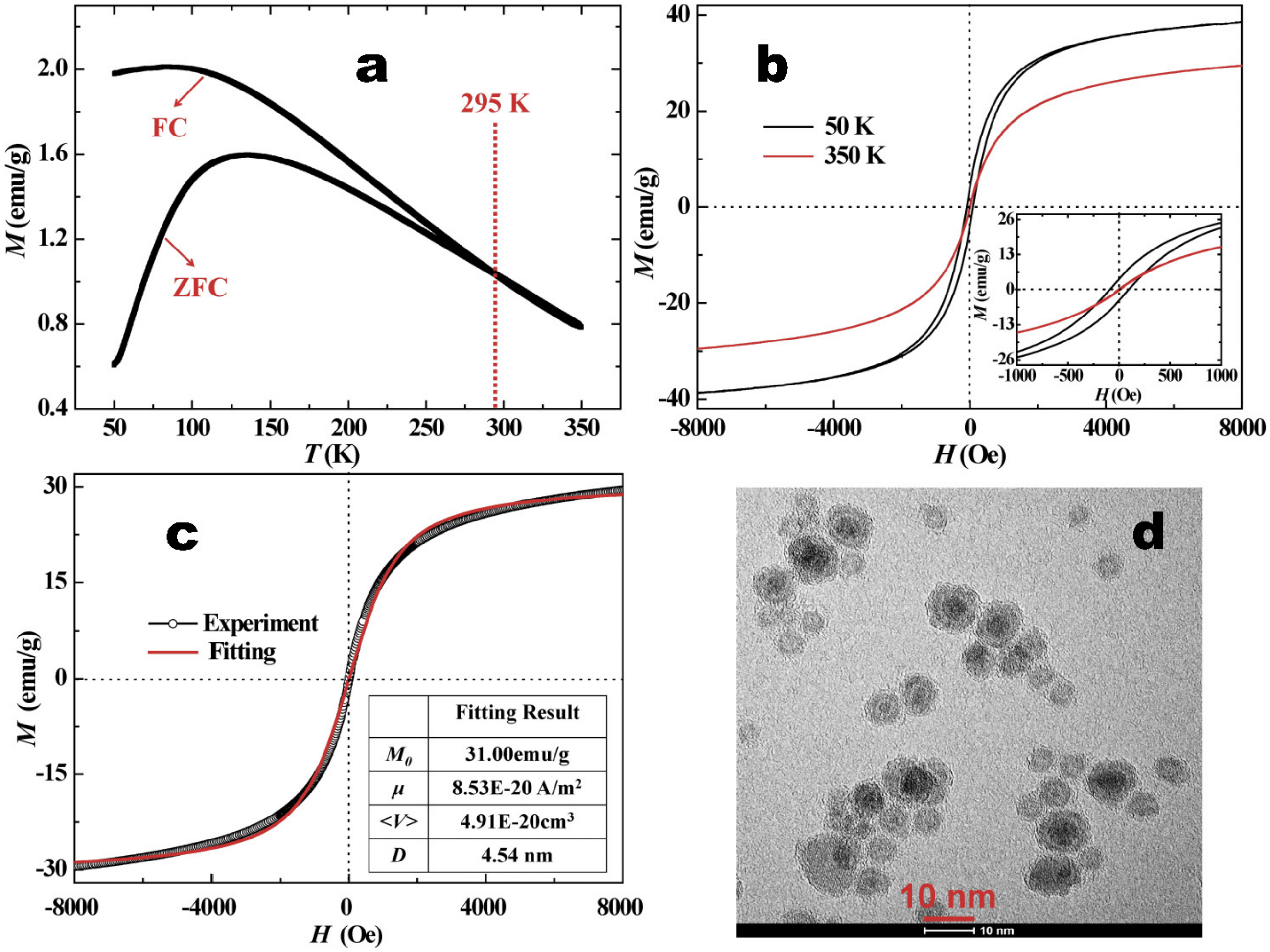

	Fitting Result
M_0	31.00emu/g
μ	8.53E-20 A/m^2
$<V>$	4.91E-20cm^3
D	4.54 nm

Extended Data Figure 8 | Experimental evidence of the superparamagnetism of the Fe nanoparticles with diameters of 2–5 nm. **a**, ZFC and FC *M*–*T* curves. **b**, *M*–*H* curves at 50 K and 350 K. **c**, Langevin fitting of the *M*–*H* curves at 350 K. **d**, TEM image of the Fe nanoparticles. The inset in **b** shows the *M*–*H* curves near zero field. The inset in **c** shows the results of the Langevin fitting.

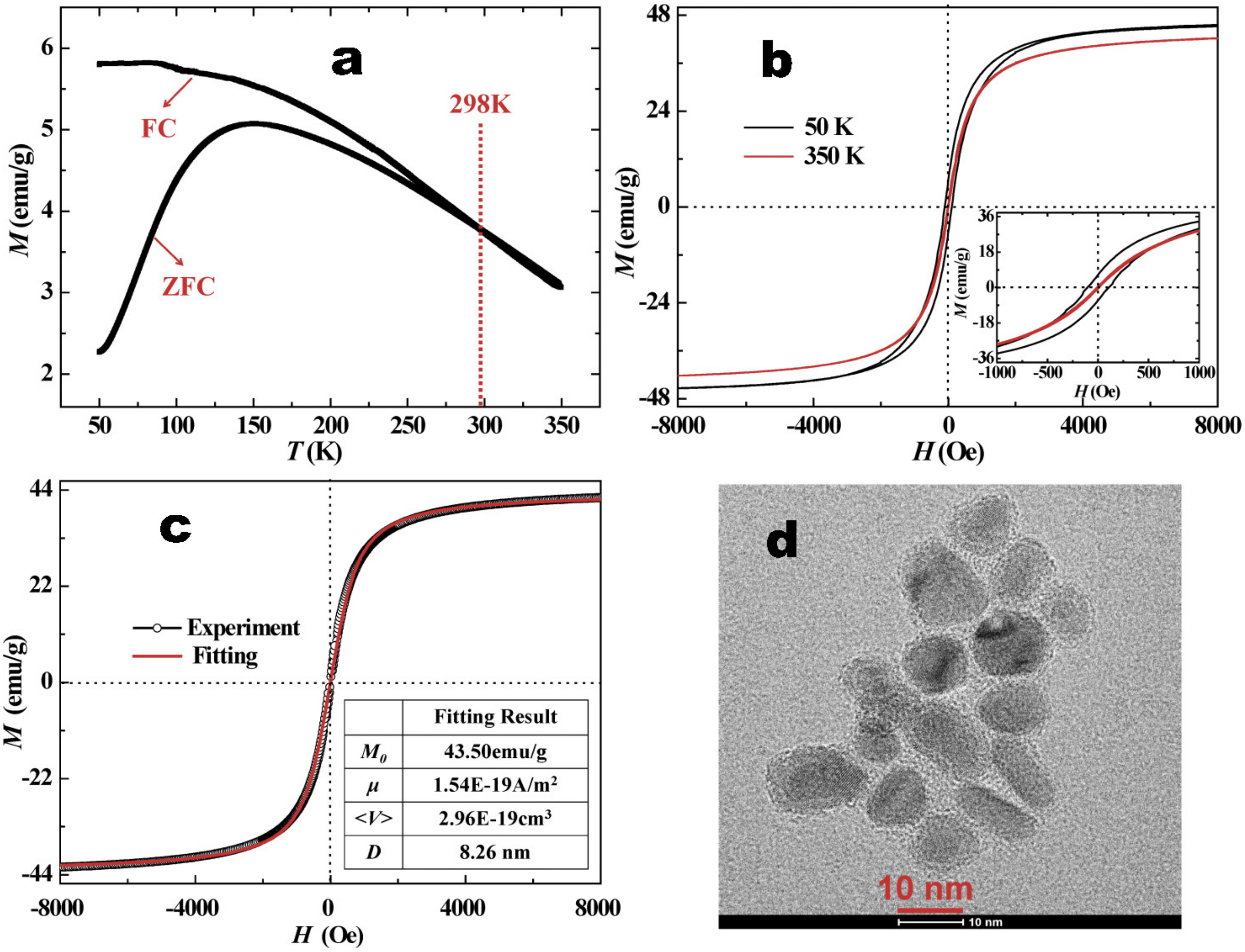

	Fitting Result
M_0	43.50emu/g
μ	1.54E-19A/m^2
<V>	2.96E-19cm^3
D	8.26 nm

Extended Data Figure 9 | Experimental evidence of the superparamagnetism of the Ni nanoparticles. **a**, ZFC and FC *M*–*T* curves. **b**, *M*–*H* curves at 50 K and 350 K. **c**, Langevin fitting of the *M*–*H* curves at 350 K. **d**, TEM image of the Ni nanoparticles with diameters of 5–10 nm. The inset in **b** shows the *M*–*H* curves near zero field. The inset in **c** shows the results of the Langevin fitting.

Extended Data Table 1 | Room-temperature charge-transport properties and scattering parameters for the first (MNC00, MNC01, MNC02 and MNC03) and second (MNC00R, MNC01R, MNC02R, MNC03R and MNC04R) batches of xCo/$Ba_{0.3}In_{0.3}Co_4Sb_{12}$ samples

Samples	x	d (mm)	R_{H^+} (10^{-2} cm^3/C)	R_{H^-} (10^{-2} cm^3/C)	R_H (10^{-2} cm^3/C)	μ_H ($cm^2/V\cdot s$)	n (10^{20} cm^{-3})	σ (10^4 S/m)	α (μV/K)	$(r_x+1)/(r_0+1)$	r_x
MNC00	0	0.86	-1.79	-1.79	-1.79	32.2	3.5	17.9	-134	1	-0.50
MNC01	0.1%	0.87	-1.52	-1.47	-1.50	29.9	4.2	19.9	-134	1.13	-0.44
MNC02	0.2%	0.81	-1.25	-1.28	-1.26	28.1	4.8	21.6	-143	1.32	-0.34
MNC03	0.3%	0.80	-1.79	-1.79	-1.79	29.9	3.5	16.6	-135	1.01	-0.50
MNC00R	0	0.86	-1.79	-1.79	-1.79	32.6	3.5	18.1	-125	1	-0.5
MNC01R	0.1%	0.88	-1.33	-1.30	-1.31	26.4	4.8	20.3	-128	1.26	-0.37
MNC02R	0.2%	0.84	-1.14	-1.09	-1.11	22.8	5.7	20.7	-143	1.58	-0.21
MNC03R	0.3%	0.90	-1.64	-1.56	-1.60	29.6	3.9	18.5	-134	1.15	-0.43
MNC04R	0.4%	0.90	-1.74	-1.66	-1.70	32.0	3.7	18.8	-137	1.14	-0.43